



Facultad de Ciencias

**On the future combination of *Planck* and  
LiteBIRD data: gravitational lensing  
effect**

Sobre la futura combinación de los datos de *Planck*  
y LiteBIRD: efecto lente gravitatorio

Trabajo de Fin de Máster  
para acceder al

**MÁSTER EN FÍSICA DE  
PARTÍCULAS Y DEL COSMOS**

**Autor:** Miguel Ruiz Granda  
**Director:** Patricio Vielva Martínez  
**Codirectora:** Patricia Diego Palazuelos

**Septiembre 2022**



# Contents

<b>Abstract/Resumen</b>	<b>III</b>
<b>Foreword</b>	<b>V</b>
<b>1 Introduction</b>	<b>1</b>
1.1 Lensing of the CMB . . . . .	2
1.1.1 Lensing potential . . . . .	2
1.1.2 Lensing of CMB temperature . . . . .	4
1.1.3 Lensing of CMB polarization . . . . .	5
1.2 Lensing reconstruction with quadratic estimators . . . . .	7
1.2.1 Quadratic estimators . . . . .	8
1.2.2 Minimum-variance estimator . . . . .	9
1.2.3 Impact of sky cuts . . . . .	10
<b>2 Methodology</b>	<b>12</b>
2.1 Simulating ideal lensed CMB maps . . . . .	12
2.1.1 Computing the CMB angular power spectra . . . . .	12
2.1.2 Correlating unlensed fields using Cholesky decomposition . . . . .	14
2.1.3 Lensing the CMB maps . . . . .	15
2.2 Observed CMB maps by different experiments . . . . .	18
2.2.1 <i>Planck</i> and LiteBIRD experiments . . . . .	19
2.2.2 Combination of <i>Planck</i> and LiteBIRD experiments . . . . .	20
2.2.3 Masking the CMB maps . . . . .	24
2.3 Reconstruction of the lensing potential . . . . .	27
2.4 Wiener filter . . . . .	28
<b>3 Results</b>	<b>30</b>

3.1	Lensing reconstruction from noisy and limited resolution experiments . . . .	30
3.1.1	Weights of the minimum-variance estimator . . . . .	32
3.1.2	Patch of the reconstructed lensing map . . . . .	33
3.1.3	Signal-to-noise ratio . . . . .	35
3.2	Impact of partial sky coverage on lensing reconstruction . . . . .	37
<b>4</b>	<b>Conclusions and future work</b>	<b>39</b>
	<b>Bibliography</b>	<b>41</b>

# Abstract

The main objective of this work is to study how we can combine the data from the Cosmic Microwave Background (CMB) experiments *Planck* and the upcoming LiteBIRD in order to improve the estimation of the gravitational lensing effect. This effect deflects the CMB photons along their path to us and it is an important cosmological probe as it traces the distribution of matter in the Universe. Along this work, CMB maps have been simulated taking into account a simplified experimental framework, including white instrumental noise, limited angular resolution, and partial sky coverage. Using the quadratic estimators from Okamoto & Hu [1], the map of the gravitational lensing potential can be reconstructed from the observed CMB maps. The results provided in this document show that combining both experiments is a great idea because they are complementary. While *Planck* has measured very precisely CMB temperature, LiteBIRD will measure CMB polarization with an unprecedented precision. Consequently, the estimated full-sky signal-to-noise ratio of the lensing potential for the combination will be of about 130, whereas for each individual experiment is approximately of 86 for *Planck* and 88 for LiteBIRD. It implies an improvement of about a 50% in the lensing potential reconstruction when combining both experiments.

**Keywords:** Cosmic Microwave Background, Cosmology, Weak Gravitational Lensing, Quadratic Estimators.

# Resumen

El objetivo principal de este trabajo es estudiar cómo combinar los datos de los experimentos de Fondo Cósmico de Microondas (FCM) *Planck* y la futura misión LiteBIRD con el fin de mejorar la estimación del efecto lente gravitacional. Este efecto deflcta los fotones del FCM a lo largo de su camino hacia nosotros y es una importante sonda cosmológica ya que traza la distribución de materia en el Universo. A lo largo de este trabajo se han simulado mapas del FCM teniendo en cuenta un marco experimental simplificado, incluyendo ruido instrumental blanco, resolución angular limitada y cobertura parcial del cielo. A partir de los mapas simulados y utilizando los estimadores cuadráticos de Okamoto & Hu [1], el mapa del potencial gravitatorio ha podido ser reconstruido. Los resultados que aparecen en este documento muestran que combinar ambos experimentos es una gran idea porque son complementarios. Mientras que *Planck* ha medido con gran precisión la temperatura del FCM, LiteBIRD medirá con una precisión sin precedentes la polarización del FCM. Consecuentemente, la razón señal-ruido estimada a cielo completo para la combinación de ambos experimentos será aproximadamente de 130, mientras que para cada experimento de forma individual se estima que es 86 para *Planck* y 88 para LiteBIRD. Esto implica una mejora del 50% en la reconstrucción del potencial al combinar ambos experimentos.

**Palabras clave:** Fondo Cósmico de Microondas, Cosmología, Efecto Lente Gravitacional Débil, Estimadores Cuadráticos.



# Foreword

This master's thesis is the result of a project under the supervision of Patricio Vielva and Patricia Diego. It has been supported by a JAE Intro 2021 grant from the Spanish National Research Council (CSIC). Due to the important computational component of this work, the Altamira Supercomputer at the Institute of Physics of Cantabria (IFCA-CSIC), member of the Spanish Supercomputing Network, was used for performing most of the simulations.

Our work aims to study how well can the gravitational lensing potential be reconstructed from CMB observations from *Planck* and the future mission LiteBIRD. To do so, we have used simulations from both experiments under a simplified experimental scheme. The novelty of our approach is in the way both data sets are combined, using always the best data available in terms of noise levels. The lensing potential is reconstructed using the quadratic estimators from Okamoto & Hu [1].

This work is structured as follows. In Chapter 1, we introduce the Cosmic Microwave Background and focus on the effect that Weak Gravitational Lensing has on the CMB. We explain how the CMB angular power spectra is affected by lensing and the correlations between multipoles introduced by this effect, which are the key of the quadratic estimators. Chapter 2 focuses on explaining how the observed CMB maps are simulated and how the lensing potential is reconstructed. It also describes the different `Python` libraries we used to do so. In Chapter 3, the results obtained from the lensing reconstruction from observed CMB maps are presented for two situations: full-sky and partial-sky coverage. Finally, in Chapter 4 the conclusions of this project and future work are described. The `Python` code developed for this project can be found at <https://github.com/miguelrgranda/lensingReconstruction>.



# Chapter 1

## Introduction

The Universe in its origin was very hot, dense, and opaque. In this early phase, radiation and matter were in thermal equilibrium, with photons continuously scattered by free electrons through Thomson scattering. As the Universe expanded, it progressively cooled down, and became transparent when it reached a temperature of around 3000 K. Radiation decoupled from matter and photons escaped.

This radiation emitted when the Universe was 375.000 years old, 13.8 billion years ago, is observed nowadays in the microwave range as an almost perfect black-body spectrum with a characteristic temperature of  $T_0 = 2.72548 \pm 0.00057$  K [2]. For that reason, it is named the Cosmic Microwave Background (CMB). The CMB radiation was discovered by Penzias and Wilson in 1965, however it was not until 1992 when the temperature fluctuations were detected with COBE.

Although the CMB is extremely homogeneous, small temperature anisotropies have been observed at the  $10^{-5}$  K level. These temperature anisotropies contain valuable information about the primordial density perturbations and the characteristics of our Universe. In particular, it can be used to constrain the cosmological parameters that appear in the standard cosmological model, named  $\Lambda$ CDM, which describes a flat Universe containing three major components: baryonic or ordinary matter, cold dark matter (weakly interacting non-relativistic matter detected only by its gravitational effects) and dark energy (consistent with a cosmological constant  $\Lambda$ , causing the current accelerated expansion of the Universe).

The existence of temperature fluctuations implies that CMB radiation must be polarized as a consequence of the directional dependence of the Thomson scattering, which was confirmed this century. Experiments such as WMAP (2001-2012) and more recently *Planck*, whose final data release is from 2018, provided precise measurements of the temperature and polarization fluctuations generated on the last scattering surface [3].

These CMB anisotropies are partly produced at the last scattering surface at redshift  $z = 1090$ , when the CMB photons escaped. We used the word partly because on their path from the last scattering surface to us, CMB photons experience several effects. For instance, the Integrated Sachs-Wolfe effect, which is a consequence of the time evolution of potential wells along the line of sight, or other second order effects like the lensing effect, which is the main topic of this project. Its main consequences are the deflection

of photons by the perturbed gravitational field, which produces changes in the pattern of CMB anisotropies, the introduction of non-Gaussianities, and the generation of a B-mode polarization signal, which is an important signal that prevents us from detecting primordial gravitational waves. The lensing effect is called a second order effect because, if the CMB was perfectly isotropic or there were no perturbations on the gravitational potential, the net effect of the deflection would vanish.

## 1.1 Lensing of the CMB

In this Section we explain how to calculate the angular power spectrum of the lensing potential and how lensing changes the shape of the CMB angular power spectra. This part is strongly based on two main references, which are the excellent review on CMB weak lensing made by Lewis and Challinor [4] and [5].

The lensing effect produces small deflections on the direction of CMB photons (weak lensing regime) and in this work we will work under the Born approximation, which consist in calculating the lensing potential gradients along the undeflected path. The mean deflection of each potential is of about  $|\boldsymbol{\alpha}| = 10^{-4}$ . Assuming that the typical size of the potential wells is about 300 Mpc (comoving) and that the distance to the last scattering surface is about 14000 Mpc, then light rays have passed through the order of 50 of such wells. If the potentials are uncorrelated we would expect a total deviation of  $\sqrt{50}|\boldsymbol{\alpha}| = 2$  arcmin. We then expect lensing to become an order unity effect on the CMB at scales  $\ell \gtrsim 3000$ .

### 1.1.1 Lensing potential

The deflection angle,  $\boldsymbol{\alpha}(\hat{\mathbf{n}})$ , of a source at conformal distance  $\chi_*$  is given in terms of the gravitational potential  $\Phi$  by

$$\boldsymbol{\alpha}(\hat{\mathbf{n}}) = -2 \int_0^{\chi_*} d\chi \frac{f_K(\chi_* - \chi)}{f_K(\chi_*)f_K(\chi)} \nabla_{\hat{\mathbf{n}}} \Phi(\chi \hat{\mathbf{n}}; \eta_0 - \chi), \quad (1.1)$$

where  $\eta_0 - \chi$  is the conformal time in which the photon was at position  $\chi \hat{\mathbf{n}}$ ,  $\nabla_{\hat{\mathbf{n}}}$  is the angular derivative, which is equivalent to the covariant derivative on the sphere defined by  $\hat{\mathbf{n}}$ , and  $f_K(\chi)$  is the angular diameter distance, where

$$f_K(\chi) = \begin{cases} K^{-1/2} \sin(K^{1/2}\chi) & \text{for } K > 0 \text{ (closed),} \\ \chi & \text{for } K = 0 \text{ (flat),} \\ |K|^{-1/2} \sinh(|K|^{1/2}\chi) & \text{for } K < 0 \text{ (open).} \end{cases} \quad (1.2)$$

Now, we define the lensing potential:

$$\phi(\hat{\mathbf{n}}) \equiv -2 \int_0^{\chi_*} d\chi \frac{f_K(\chi_* - \chi)}{f_K(\chi_*)f_K(\chi)} \Phi(\chi \hat{\mathbf{n}}; \eta_0 - \chi), \quad (1.3)$$

so that the deflection angle is given by  $\nabla_{\hat{\mathbf{n}}}\phi(\hat{\mathbf{n}})$ .

For the CMB, we can approximate recombination as being instantaneous and described by a single plane at  $\chi = \chi_*$ . We neglect the very small effect of late times sources, including reionization. For scales where  $\Phi$  is Gaussian, the lensing potential is also Gaussian. On smaller scales, non-linear evolution can introduce non-Gaussianities, however, we are not considering this in this work.

For a flat Universe,  $f_K(\chi) = \chi$ , and for simplicity we are going to assume flatness hereafter. As the reader may notice, a divergent term  $1/\chi$  arises in equations (1.1) and (1.3) near  $\chi = 0$ . However, it only affects the monopole of the lensing potential, which is related to the mean value across the sky and does not contribute to the deflection angle. Therefore, we can set the monopole term to zero and the remaining multipoles would be finite, meaning that the lensing potential field is well defined.

As a Gaussian field, the lensing potential is fully characterized by its power spectrum. Next, we will derive the lensing potential power spectrum in terms of the power spectrum of the gravitational potential.

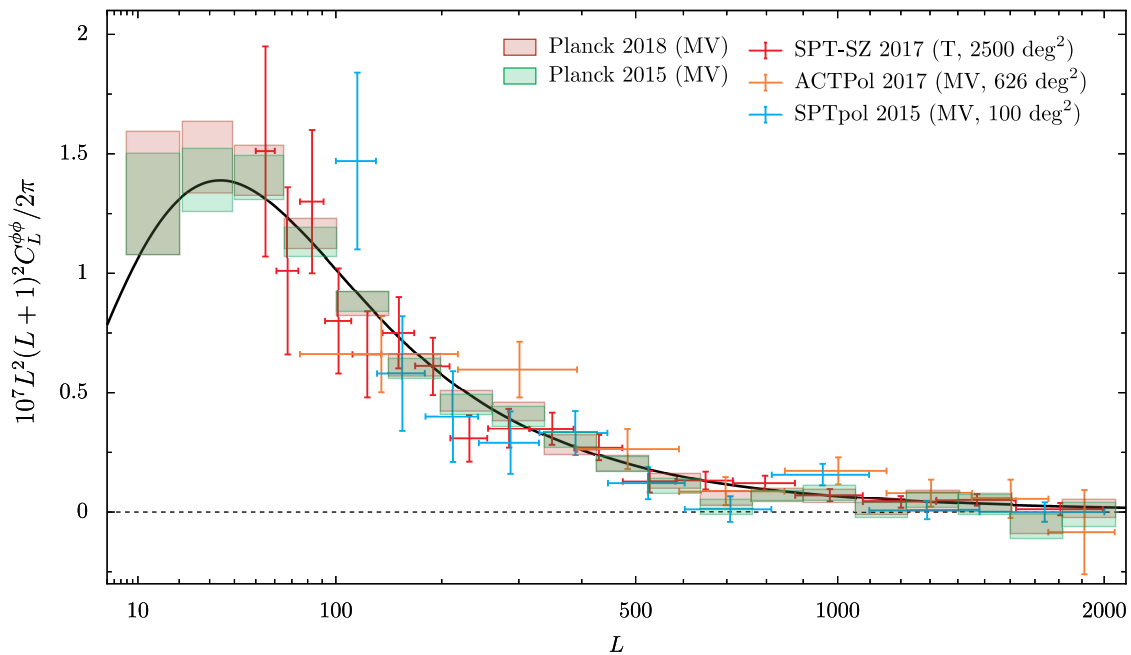


Figure 1.1: *Planck 2018 lensing power spectrum band powers (pink boxes) and the 2015 analysis band powers (green boxes). Also shown are recent measurements by the ACTPol [6], SPTpol [7], and SPT-SZ [8] collaborations. The black line shows the lensing potential power spectrum for the  $\Lambda$ CDM best-fit parameters to the Planck 2018  $TT, TE, EE+lowE$ . Figure from [9].*

First, we expand the lensing potential in spherical harmonics:

$$\phi(\hat{\mathbf{n}}) = \sum_{\ell=0}^{+\infty} \sum_{m=-\ell}^{+\ell} \phi_{\ell m} Y_{\ell m}(\hat{\mathbf{n}}), \quad (1.4)$$

where the  $\phi_{\ell m}$  complex coefficients are Gaussian distributed with zero mean,  $\langle \phi_{\ell m} \rangle = 0$ ,

and non-zero variance,  $\langle \phi_{\ell m} \phi_{\ell' m'}^* \rangle = \delta_{\ell\ell'} \delta_{mm'} C_\ell^{\phi\phi}$ . The monopole term is set to zero, so  $\phi_{00} = 0$  and normally the summation on  $\ell$ s is restricted up to a maximum value  $\ell_{max}$  (instead of going to infinity) due to experimental limitations such as spatial resolution.

The variance of the spherical harmonic coefficients,  $C_\ell^{\phi\phi}$ , is called the lensing angular power spectrum and is given by

$$C_\ell^{\phi\phi} = 16\pi \int \frac{dk}{k} \mathcal{P}_{\mathcal{R}}(k) \left[ \int_0^{\chi_*} d\chi \left( \frac{\chi_* - \chi}{\chi_* \chi} \right) j_\ell(k\chi) T_\Phi(k, \eta_0 - \chi) \right]^2, \quad (1.5)$$

where  $T_\Phi(k, \eta_0 - \chi)$  is a transfer function so that  $\Phi(\mathbf{k}; \eta_0 - \chi) = T_\Phi(k, \eta_0 - \chi) \mathcal{R}(\mathbf{k})$ , being  $\mathcal{R}(\mathbf{k})$  the primordial comoving perturbation, and the primordial power spectrum is  $\mathcal{P}_{\mathcal{R}}(k)$ , usually expressed in a power-law form:

$$\mathcal{P}_{\mathcal{R}}(k) = A_s \left( \frac{k}{k_*} \right)^{n_s - 1}, \quad (1.6)$$

where  $k_* = 0.05 \text{ Mpc}^{-1}$ ,  $A_s$  is the scalar amplitude, and  $n_s$  is the scalar spectral index.

In Figure 1.1, the lensing power spectrum measured by *Planck* and other CMB experiments are shown.

### 1.1.2 Lensing of CMB temperature

The purpose of this Subsection is to understand how the CMB temperature power spectrum is affected by lensing. The lensing effect introduces non-Gaussianities and changes the shape of the temperature power spectrum by smoothing the peaks and troughs in the small angular scales. Although being a second-order effect, it has to be correctly taken into account to obtain accurate cosmological parameter constraints from CMB observations.

#### Flat-sky approximation for CMB temperature

As we are mostly interested in small scales, we adopt a flat-sky approximation to obtain the lensed temperature power spectrum. For  $\ell \gtrsim 100$ , which corresponds to angular scales of less than about  $2^\circ$ , we can neglect the curvature of the sphere of directions and consider it as a normal plane to  $\hat{\mathbf{e}}_z$ . In this approximation, we can replace the spherical harmonics by exponentials.

$$Y_{\ell m}(\hat{\mathbf{n}}) \rightarrow \frac{1}{2\pi} e^{i\boldsymbol{\ell} \cdot \mathbf{x}}, \quad (1.7)$$

where  $\mathbf{x}$  is a small vector in the plane normal to  $\hat{\mathbf{e}}_z$  and  $\boldsymbol{\ell} = \ell(\cos \varphi_\ell, \sin \varphi_\ell)$  is a vector in the Fourier plane. In this approximation the magnetic quantum number  $m$  is replaced by the continuous direction of the vector  $\boldsymbol{\ell}$ . This means we are switching from a spherical harmonics transform to a Fourier transform of the temperature anisotropy map,  $T$ :

$$T(\hat{\mathbf{n}}) = \sum_{\ell=0}^{+\infty} \sum_{m=-\ell}^{+\ell} t_{\ell m} Y_{\ell m}(\hat{\mathbf{n}}) \quad \longrightarrow \quad T(\mathbf{x}) = \frac{1}{2\pi} \int d^2\boldsymbol{\ell} T(\boldsymbol{\ell}) e^{i\boldsymbol{\ell} \cdot \mathbf{x}}. \quad (1.8)$$

The temperature fluctuations are assumed to be statistically isotropic, which means that any statistical average cannot depend on the position or orientation on the sky where

it is evaluated. The correlation function of the temperature at two points,  $\xi$ , can only depend on the separation between the points, and the power spectrum for the temperature field is diagonal in  $\ell$ :

$$\langle T(\mathbf{x})T(\mathbf{x}') \rangle = \xi(|\mathbf{x} - \mathbf{x}'|), \quad \langle T(\boldsymbol{\ell})T^*(\boldsymbol{\ell}') \rangle = \delta(\boldsymbol{\ell} - \boldsymbol{\ell}')C_{\ell}^{TT}. \quad (1.9)$$

### Approximation for small deflection angles for CMB temperature

To derive an expression for the lensed temperature power spectrum we will use an approximation for small deflection angles. As argued at the beginning of this document, for  $\ell > 3000$  the deflection angle is comparable to the angular separation between points, and therefore this approximation is not longer valid.

In the first-order approximation, the deflection angles have zero curl and can be described as the gradient of a potential,  $\boldsymbol{\alpha} = \nabla\phi$ . The lensing effect changes the direction in which the photon is received, which can be interpreted as a remapping of the unlensed temperature map:

$$\tilde{T}(\mathbf{x}) = T(\mathbf{x} + \nabla\phi), \quad (1.10)$$

where  $\tilde{T}(\mathbf{x})$  is the lensed temperature anisotropy and  $T(\mathbf{x})$  is the unlensed temperature anisotropy.

The small deflection angle approximation mentioned before consists in a Taylor series expansion truncated at second order,

$$\tilde{T}(\mathbf{x}) = T(\mathbf{x} + \nabla\phi) \approx T(\mathbf{x}) + \nabla^a\phi(\mathbf{x})\nabla_a T(\mathbf{x}) + \frac{1}{2}\nabla^a\phi(\mathbf{x})\nabla^b\phi(\mathbf{x})\nabla_a\nabla_b T(\mathbf{x}). \quad (1.11)$$

Neglecting the correlation between  $T$  and  $\phi$  coming from the Integrated Sachs-Wolfe (ISW) effect we get the following equation [10],

$$\tilde{C}_{\ell}^{TT} \approx (1 - \ell^2 R^{\phi})C_{\ell}^{TT} + \frac{1}{4\pi^2} \int d^2\ell' (\boldsymbol{\ell}' \cdot (\boldsymbol{\ell} - \boldsymbol{\ell}'))^2 C_{|\boldsymbol{\ell} - \boldsymbol{\ell}'|}^{\phi\phi} C_{\ell'}^{TT}, \quad (1.12)$$

where we have defined half the total deflection angle as

$$R^{\phi} \equiv \frac{1}{2}\langle \boldsymbol{\alpha}^2 \rangle = \frac{1}{4\pi} \int_0^{\infty} d\ell' \ell'^3 C_{\ell'}^{\phi\phi}, \quad (1.13)$$

whose value is for typical models  $R^{\phi} \sim 3 \times 10^{-7}$ , corresponding to an rms deflection of  $\sim 2.7$  arcmin. The integral term in equation (1.12) smooths the peaks of the unlensed power spectrum, which is the main qualitative effect that we can observe on the temperature spectrum pattern at high  $\ell$ .

#### 1.1.3 Lensing of CMB polarization

In this Subsection we study how CMB polarization is affected by lensing. There are two lensing contributions to the observed CMB polarized sky. First, as occurs for temperature, lensing re-maps the observed CMB photons coming from  $\hat{\mathbf{n}}' = \hat{\mathbf{n}} + \boldsymbol{\alpha}$ , where  $\hat{\mathbf{n}}$  is the direction in which they have been observed. Second, the propagation of the polarization

basis along the perturbed line of sight  $\hat{\mathbf{n}}$  at last scattering will be rotated in comparison to an unlensed basis transported along  $\hat{\mathbf{n}} + \boldsymbol{\alpha}$ . To lowest order, this means that the orientation in the observed direction  $\hat{\mathbf{n}}$  and in the lensed direction  $\hat{\mathbf{n}}'$  are the same if they are determined with respect to a basis that is parallel transported from  $\hat{\mathbf{n}}$  to  $\hat{\mathbf{n}}'$ . In the flat sky approximation, this basically means that we have to measure polarization in both points with respect to the same basis  $(\hat{\mathbf{e}}_1, \hat{\mathbf{e}}_2)$ . The effect of lensing for polarization can now be handled in a similar way as temperature.

### Flat-sky approximation for CMB polarization

As for temperature, we will use the flat-sky approximation. In the flat-sky approximation, the spin-2 spherical harmonics are given by

$$\pm_2 Y_{\ell m}(\mathbf{x}) \rightarrow -e^{\pm 2i\varphi_\ell} e^{i\boldsymbol{\ell} \cdot \mathbf{x}}, \quad (1.14)$$

where  $\varphi_\ell$  is the angle which  $\boldsymbol{\ell}$  encloses with the  $\mathbf{x}$  axis.

We expand now the polarization field as

$$(Q \pm iU)(\mathbf{x}) = -\frac{1}{2\pi} \int d^2\boldsymbol{\ell} (E(\boldsymbol{\ell}) \pm iB(\boldsymbol{\ell})) e^{\pm 2i\varphi_\ell} e^{i\boldsymbol{\ell} \cdot \mathbf{x}}, \quad (1.15)$$

where  $Q$  and  $U$  are the Stokes parameters describing linear polarization.

### Approximation for small deflection angles for CMB polarization

The approximation for small deflection angles, as explained for CMB temperature, is not valid for all scales. It only holds when considering angular scales much larger than the deflection angle ( $\ell \lesssim 3000$ ). Nevertheless, under the small deflection angle approximation, we can qualitatively understand how lensing affects CMB polarization.

While CMB temperature is a scalar field, the CMB polarization is a tensor field characterized by a trace-free symmetric polarization tensor  $P_{ab}$ . For some choice of orthonormal basis  $(\hat{\mathbf{e}}_1, \hat{\mathbf{e}}_2)$ , the components for the polarization tensor are

$$P_{ab} = \frac{1}{2} \begin{pmatrix} Q & U \\ U & -Q \end{pmatrix}. \quad (1.16)$$

As for temperature anisotropies, we start by expanding the polarization tensor in the deflection angle up to second order,

$$\tilde{P}_{ab}(\mathbf{x}) = P_{ab}(\mathbf{x} + \nabla\phi) \approx P_{ab}(\mathbf{x}) + \nabla^c\phi \nabla_c P_{ab}(\mathbf{x}) + \frac{1}{2} \nabla^c\phi \nabla^d\phi \nabla_c \nabla_d P_{ab}(\mathbf{x}). \quad (1.17)$$

Since parallel-transporting in the flat sky means keeping the polarization basis  $\mathbf{e}_\pm = \hat{\mathbf{e}}_1 \pm i\hat{\mathbf{e}}_2$  constant, the same expression is valid for  $Q \pm iU$ .

In the flat-sky approximation and, for statistically isotropic fields, the unlensed power spectra of  $EE$ ,  $BB$  and  $TE$  are given by

$$\begin{aligned} \langle E(\boldsymbol{\ell}) E^*(\boldsymbol{\ell}') \rangle &= \delta(\boldsymbol{\ell} - \boldsymbol{\ell}') C_\ell^{EE}, \\ \langle B(\boldsymbol{\ell}) B^*(\boldsymbol{\ell}') \rangle &= \delta(\boldsymbol{\ell} - \boldsymbol{\ell}') C_\ell^{BB}, \\ \langle T(\boldsymbol{\ell}) E^*(\boldsymbol{\ell}') \rangle &= \delta(\boldsymbol{\ell} - \boldsymbol{\ell}') C_\ell^{TE}. \end{aligned} \quad (1.18)$$

We have assumed that statistical parity invariance holds, so that  $B$  is uncorrelated with  $T$  or  $E$ . Now, after keeping only lowest-order terms in  $C_\ell^{\phi\phi}$ , the  $EE$ ,  $BB$  and  $TE$  lensed power spectra are given by

$$\begin{aligned}
 \tilde{C}_\ell^{EE} &= (1 - \ell^2 R^\phi) C_\ell^{EE} \\
 &\quad + \frac{1}{4\pi^2} \int d^2\ell' (\ell' \cdot (\ell - \ell'))^2 C_{|\ell-\ell'|}^{\phi\phi} [C_{\ell'}^{EE} \cos^2 2(\varphi_{\ell'} - \varphi_\ell) + C_{\ell'}^{BB} \sin^2 2(\varphi_{\ell'} - \varphi_\ell)], \\
 \tilde{C}_\ell^{BB} &= (1 - \ell^2 R^\phi) C_\ell^{BB} \\
 &\quad + \frac{1}{4\pi^2} \int d^2\ell' (\ell' \cdot (\ell - \ell'))^2 C_{|\ell-\ell'|}^{\phi\phi} [C_{\ell'}^{EE} \sin^2 2(\varphi_{\ell'} - \varphi_\ell) + C_{\ell'}^{BB} \cos^2 2(\varphi_{\ell'} - \varphi_\ell)], \\
 \tilde{C}_\ell^{TE} &= (1 - \ell^2 R^\phi) C_\ell^{TE} + \frac{1}{4\pi^2} \int d^2\ell' (\ell' \cdot (\ell - \ell'))^2 C_{|\ell-\ell'|}^{\phi\phi} C_{\ell'}^{TE} \cos 2(\varphi_{\ell'} - \varphi_\ell),
 \end{aligned} \tag{1.19}$$

where  $R^\phi$  is given by equation (1.13).

One of the most interesting aspects of equation (1.19) is the fact that, even in the situation where no primordial B-mode polarization exists,  $C_\ell^{BB} = 0$  (purely scalar perturbations), lensing induces a non-zero B-mode spectrum given by

$$\tilde{C}_\ell^{BB} = \frac{1}{4\pi^2} \int d^2\ell' (\ell' \cdot (\ell - \ell'))^2 C_{|\ell-\ell'|}^{\phi\phi} C_{\ell'}^{EE} \sin^2 2(\varphi_{\ell'} - \varphi_\ell). \tag{1.20}$$

This has crucial implications in the detectability of the primordial gravitational wave (tensor modes) background via the B-mode signal by future experiments. In order to detect this background, we will need to first characterize the contribution from lensing and this is one important reason why understanding lensing is critical in CMB science.

## 1.2 Lensing reconstruction with quadratic estimators

In the previous Section, we have introduced how the temperature and polarization angular power spectra are modified by the effect of lensing. Additionally, the lensing effect produces higher-order correlations between the multipole moments. In this Section, we explain how to measure the lensing potential using quadratic combinations of the CMB fields to form the so-called quadratic estimators. This is explained in Subsection 1.2.1. In Subsection 1.2.2, we explain how to combine the different quadratic estimators to minimize the reconstruction noise. Finally, in Subsection 1.2.3 we discuss the impact of partial sky coverage on the quadratic estimators.

The flat-sky approximation was used in the previous Section for simplicity. However, most of the lensing power is concentrated at  $\ell < 10^2$  where this approximation fails. For that reason, a treatment incorporating the curvature of the sky is preferable and will be used hereafter. This introduces an additional level of complexity because it requires working with spherical harmonics functions instead of the much easier Fourier's exponentials. For simplicity, we will skip the underlying mathematics in this Section, but a detailed treatment can be found in [10].

### 1.2.1 Quadratic estimators

The unlensed CMB spherical harmonic coefficients  $X_{\ell m}$  are assumed to be Gaussian and statistically isotropic, so that the statistical properties are characterized by the angular power spectra,

$$\langle X_{\ell m} Y_{\ell' m'}^* \rangle = \delta_{\ell\ell'} \delta_{mm'} C_{\ell}^{XY}, \quad (1.21)$$

where  $X, Y \in \{T, E, B\}$ .

Due to the effect of lensing by a fixed deflection field, the covariance acquires off-diagonal terms and becomes

$$\langle \tilde{X}_{\ell m} \tilde{Y}_{\ell' m'}^* \rangle |_{\phi} = C_{\ell}^{XY} \delta_{\ell\ell'} \delta_{m-m'} (-1)^m + \sum_{LM} (-1)^M \begin{pmatrix} \ell & \ell' & L \\ m & m' & -M \end{pmatrix} f_{\ell L \ell'}^{XY} \phi_{LM}, \quad (1.22)$$

where the matrix corresponds to the Wigner  $3-j$  symbols and  $f_{\ell L \ell'}^{XY}$  are weights for the different quadratic pairs which depend on the lensed angular power spectra.

An estimator for the lensing potential  $\hat{\phi}_{\ell m}^{XY}$  can be built using the existing correlations produced by lensing. It is expressed as a weighted sum over multipole pairs, where the weights minimize the variance of the estimator, leading to the following equation:

$$\hat{\phi}_{\ell m}^{XY} = \frac{A_{\ell}^{XY}}{\ell(\ell+1)} \sum_{\ell_1 m_1} \sum_{\ell_2 m_2} (-1)^M \begin{pmatrix} \ell_1 & \ell_2 & L \\ m_1 & m_2 & -M \end{pmatrix} f_{\ell_1 L \ell_2}^{XY} h^{XY} \frac{a_{\ell_1 m_1}^X}{\hat{C}_{\ell_1}^{XX}} \frac{a_{\ell_2 m_2}^Y}{\hat{C}_{\ell_2}^{YY}}, \quad (1.23)$$

where  $A_{\ell}^{XY}$  is a normalization factor,  $a_{\ell_1 m_1}^X$  and  $a_{\ell_2 m_2}^Y$  are the corresponding spherical harmonics coefficients, and  $\hat{C}_{\ell_1}^X$  and  $\hat{C}_{\ell_2}^Y$  their angular power spectra. Finally,

$$h^{XY} = \begin{cases} \frac{1}{2}, & \text{if } X = Y, \\ 1, & \text{otherwise.} \end{cases} \quad (1.24)$$

The covariance of the recovered lensing potential is given by the following equation:

$$\langle \hat{\phi}_{\ell m}^{XY} \hat{\phi}_{\ell' m'}^{X'Y'*} \rangle = \delta_{\ell\ell'} \delta_{mm'} \left[ C_{\ell}^{\phi\phi} + N_{\ell}^{XYX'Y'} \right], \quad (1.25)$$

where  $N_{\ell}^{XYX'Y'}$  is the reconstruction noise. In this work we will only take into consideration the zeroth order bias, which is the one with the highest impact and present even in the absence of lensing. It causes a positive bias for the whole multipole range. There are other higher order biases, for instance, the first order bias, which introduces a small positive bias at small scales, and the second order bias, introducing a small negative bias at large scales [11]. Both of them will be considered in future work.

As shown in [1], the reconstruction noise for  $XY = X'Y'$  corresponds to the normalization factor,

$$N_{\ell}^{XYXY} = A_{\ell}^{XY}. \quad (1.26)$$

Although a full derivation of these equations is not provided, this Section introduces all the basic notions necessary for the reconstruction of the lensing potential. A more detailed explanation can be found in [1] and [12].

### 1.2.2 Minimum-variance estimator

In this Section, we deal with the problem of combining the different quadratic estimators  $\hat{\phi}_{\ell m}^X$ , where  $X \in \{TT, EE, TE, TB, EB\}$ , to minimize the reconstruction noise. The objective is to obtain a quadratic estimator of minimum variance,  $\hat{\phi}_{\ell m}^{MV}$ , expressed as the weighted sum of the quadratic estimators from the different channels:

$$\hat{\phi}_{\ell m}^{MV} = \sum_X w_\ell^X \hat{\phi}_{\ell m}^X. \quad (1.27)$$

The problem is traduced into the optimization problem  $(MV)_\ell$  in which we want to minimize the variance of the weighted sum of equation (1.27):

$$(MV)_\ell \begin{cases} \text{Minimize Var} \left[ \sum_X w_\ell^X \hat{\phi}_{\ell m}^X \right] = \sum_{X,Y} w_\ell^X w_\ell^Y \text{Cov} \left[ \hat{\phi}_{\ell m}^X, \hat{\phi}_{\ell m}^Y \right], \\ w_\ell^X \in \mathbb{R} \text{ for each } X \in \{TT, EE, TE, TB, EB\}, \\ \text{Subject to: } \sum_X w_\ell^X = 1. \end{cases} \quad (1.28)$$

The covariance matrix of the lensing reconstruction has the following shape:

$$\text{Cov} \left[ \hat{\phi}_{\ell m}^X, \hat{\phi}_{\ell m}^Y \right] = C_\ell^{\phi\phi} + N_\ell^{XY}, \quad (1.29)$$

where

$$N_\ell = \begin{pmatrix} N_\ell^{TTTT} & N_\ell^{TTTE} & N_\ell^{TTTE} & 0 & 0 \\ N_\ell^{TTTE} & N_\ell^{TETE} & N_\ell^{TEEE} & 0 & 0 \\ N_\ell^{TTTE} & N_\ell^{TEEE} & N_\ell^{EEEE} & 0 & 0 \\ 0 & 0 & 0 & N_\ell^{TBTB} & N_\ell^{TBEB} \\ 0 & 0 & 0 & N_\ell^{TBEB} & N_\ell^{EBEB} \end{pmatrix}. \quad (1.30)$$

Substituting equation (1.29) into equation (1.28), the objective function, i.e., the function we want to minimize, reduces to

$$\sum_{X,Y} w_\ell^X w_\ell^Y \text{Cov} \left[ \hat{\phi}_{\ell m}^X, \hat{\phi}_{\ell m}^Y \right] = \sum_{X,Y} w_\ell^X w_\ell^Y (C_\ell^{\phi\phi} + N_\ell^{XY}) = C_\ell^{\phi\phi} + \sum_{X,Y} w_\ell^X w_\ell^Y N_\ell^{XY}. \quad (1.31)$$

The last equality comes from the normalization constraint of  $(MV)_\ell$ , from which it can be derived that

$$\sum_X w_\ell^X = 1 \Rightarrow \left( \sum_X w_\ell^X \right)^2 = \sum_{X,Y} w_\ell^X w_\ell^Y = 1 \Rightarrow \sum_{X,Y} w_\ell^X w_\ell^Y C_\ell^{\phi\phi} = C_\ell^{\phi\phi}. \quad (1.32)$$

Note that the value of the first term of equation (1.31),  $C_\ell^{\phi\phi}$ , is constant for any weights. Then it can be eliminated from the objective function. This leads to an equivalent problem presented in equation (1.33) which has the same solution.

$$(MV)_\ell \begin{cases} \text{Minimize } \sum_{X,Y} w_\ell^X w_\ell^Y N_\ell^{XY}, \\ w_\ell^X \in \mathbb{R} \text{ for each } X \in \{TT, EE, TE, TB, EB\}, \\ \text{Subject to: } \sum_X w_\ell^X = 1. \end{cases} \quad (1.33)$$

The problem expressed in equation (1.33) is a quadratic optimization problem. Using the Lagrange multiplier theorem, the optimal values of the  $\ell$ -dependent weights can be derived [1]:

$$w_\ell^X = \frac{\sum_Y (N_\ell^{-1})^{XY}}{N_\ell^{MV}} \text{ where } N_\ell^{MV} = \sum_X \sum_Y (N_\ell^{-1})^{XY}. \quad (1.34)$$

The solution of  $(MV)_\ell$  verifies the normalization condition imposing that the sum of the weights is equal to one. However, the weights are not bounded, i.e., they can take negative values or values above one. An example of this is presented in Subsection 3.1.1 and it should not surprise the reader.

Finally, the reader might have noticed that the quadratic estimator  $\phi_{\ell m}^{BB}$  has not been considered. The underlying reason is the little power of the B-mode power spectrum, which implies that it cannot provide much information and it can be safely ignored.

### 1.2.3 Impact of sky cuts

In the presence of a mask, applying the quadratic estimator leads to a biased reconstruction. The expectation of the lensing quadratic estimator is

$$\langle \hat{\phi}_{\ell m} \rangle = \sum_{\lambda\mu} M_{\ell m}^{\lambda\mu} \phi_{\lambda\mu} + \phi_{\ell m}^{MF}, \quad (1.35)$$

where  $M_{\ell m}^{\lambda\mu}$  is a coupling matrix which depends on the mask and  $\phi_{\ell m}^{MF}$  is a spherical harmonic coefficient of the mask mean field. The variance of the quadratic estimator is given by

$$\langle \hat{\phi}_{\ell m} \hat{\phi}_{\ell m}^* \rangle = \sum_{\lambda} M_{\ell m}^{\lambda} C_{\lambda}^{\phi\phi} + N_{\ell m}^M + C_{\ell}^{MF}, \quad (1.36)$$

where  $M_{\ell m}^{\lambda}$  is a coupling matrix which depends also on the mask,  $N_{\ell m}^M$  is a reconstruction noise depending on the structure of the mask, and  $C_{\ell}^{MF}$  is the angular power spectra of the mask mean field.

The mask mean field is present even in the absence of lensing and it is produced by the effect of the mask. For sufficiently apodized masks (see Subsection 2.2.3 for further details), the coupling matrices are essentially diagonal. In this situation, the effect of the coupling matrix is just a normalization factor:

$$\langle \hat{\phi}_{\ell m}^{XY} \hat{\phi}_{\ell' m'}^{X'Y'*} \rangle = \delta_{\ell\ell'} \delta_{mm'} \left( f_{gal,4} \left[ C_{\ell}^{\phi\phi} + N_{\ell}^{XYX'Y'} \right] + C_{\ell}^{MF} \right), \quad (1.37)$$

where

$$f_{gal,4} = \frac{1}{N_{pix}} \sum_i w_i^4, \quad (1.38)$$

$w_i$  corresponds to the value of the apodized mask at the pixel  $i$ ,  $N_{pix}$  is the number of pixels of the map, and  $N_\ell^{XYX'Y'}$  is the reconstruction noise corresponding to the full-sky scenario of Subsection 1.2.1.

The effect of the mask mean field bias can be estimated using a Monte Carlo procedure and subtracted from the quadratic estimator. However, it is out of the scope of this project and we will leave it for a future work. A more detailed explanation of this can be found in [13].

## Chapter 2

# Methodology

In this Chapter we focus on explaining how the simulated CMB maps for *Planck*, Lite-BIRD, and the combination of them are produced. We have considered idealized experiments only affected by limited angular resolution, instrumental noise, and partial sky coverage. In Sections 2.3 and 2.4, we introduce how we estimate the lensing potential using quadratic estimators on the CMB maps and the Wiener filter.

### 2.1 Simulating ideal lensed CMB maps

In this Section we detail how the simulated lensed CMB maps are obtained and explain the different techniques applied. The simulation pipeline has 3 steps. First, in Subsection 2.1.1 we compute the theoretical CMB angular power spectra. Secondly, in Subsection 2.1.2 we generate correlated unlensed CMB maps using the Cholesky decomposition technique. Finally, in Subsection 2.1.3 we explain how the simulated unlensed CMB maps are lensed.

#### 2.1.1 Computing the CMB angular power spectra

We have used the Cosmic Linear Anisotropy Solving System (CLASS)<sup>1</sup> [14] Boltzmann code to compute the CMB angular power spectra. It is written in `C`, but it is possible to execute through `Python` thanks to the existence of a `Python` wrapper.

We have used the mean values of the cosmological parameters provided by the *Planck* experiment [15] from TT,TE,EE+lowE+lensing data and assumed  $r = 0$  to compute the unlensed angular power spectra up to  $\ell_{max} = 3500$  and the lensed angular power spectra up to  $\ell_{max} = 2500$ . The one thousand multipole difference between the lensed and unlensed angular power spectra is required to precisely compute the lensed angular power spectra and for an accurate lensing of the CMB maps. Lensing the maps requires knowing information about smaller scales described at multipoles higher than  $\ell_{max} = 2500$ . Non-linear corrections are computed using the `halofit` [16] software. In the simulation of the CMB maps only the unlensed angular power spectra are required. However, the lensed power spectra is very useful for comparison purposes and will be required in the

---

<sup>1</sup><http://www.class-code.net/>

computation of the quadratic estimators of the lensing potential. In the Figures 2.1 and 2.2 the computed theoretical unlensed and lensed CMB angular power spectra are plotted.

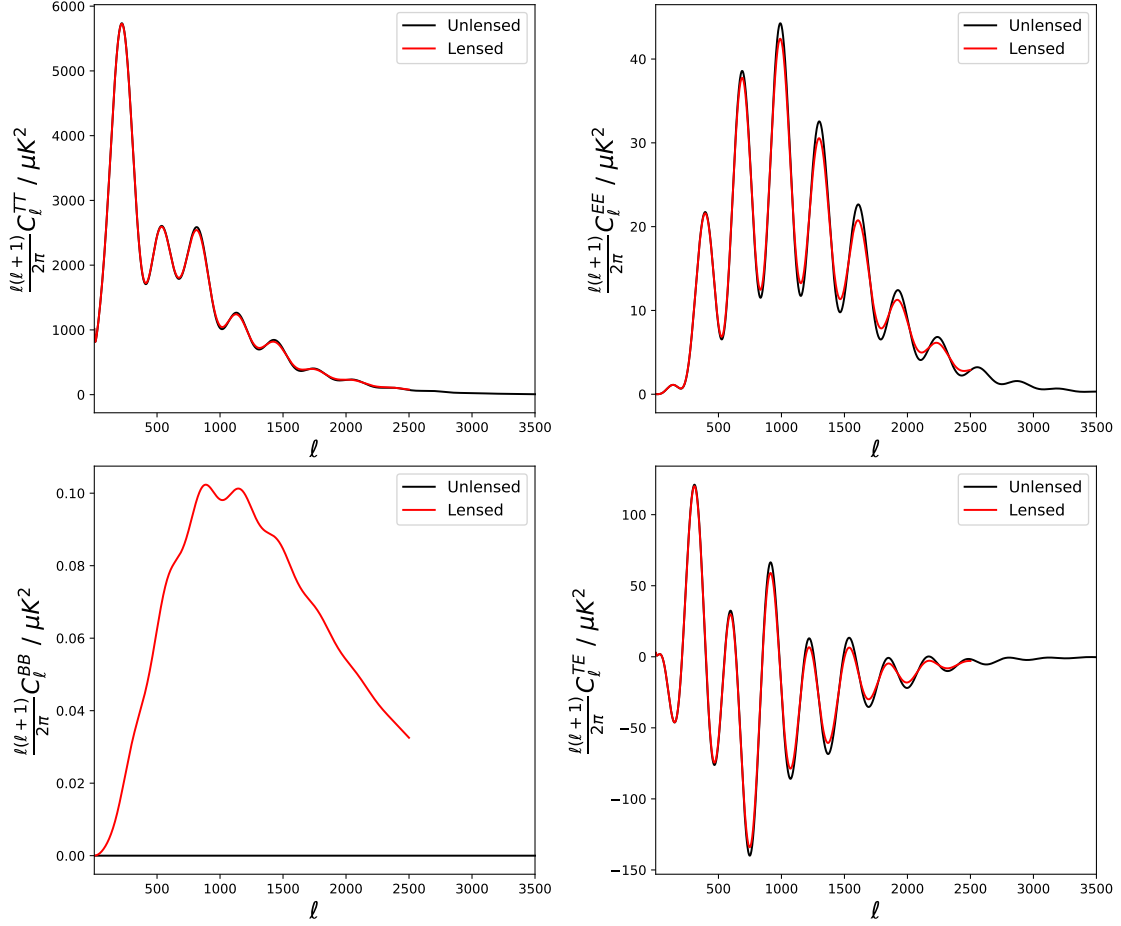


Figure 2.1: The unlensed and lensed  $TT$ ,  $TE$ ,  $EE$  and  $BB$  angular power spectra computed with *CLASS* using Planck 2018  $TT, TE, EE + \text{low}E + \text{lensing}$  cosmological parameters.

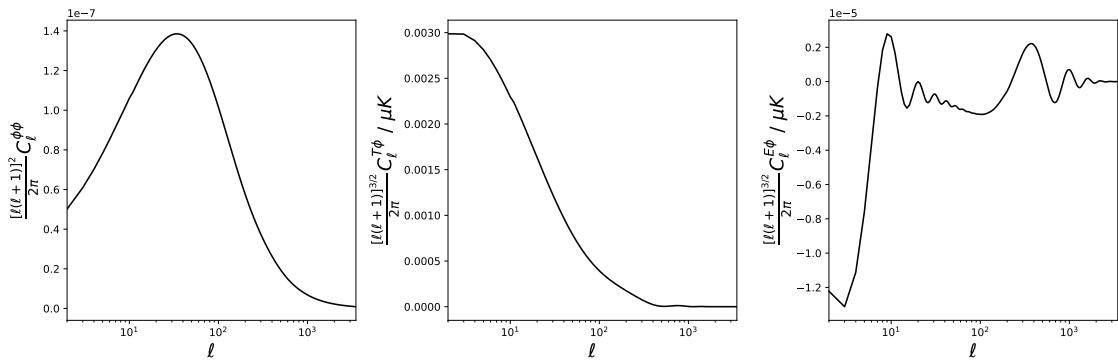


Figure 2.2: The unlensed  $\phi\phi$ ,  $T\phi$  and  $E\phi$  angular power spectra computed with *CLASS* using Planck 2018  $TT, TE, EE + \text{low}E + \text{lensing}$  cosmological parameters.

### 2.1.2 Correlating unlensed fields using Cholesky decomposition

In this Subsection, we explain how to generate random realizations of spherical harmonic coefficients for the unlensed CMB temperature and E-mode polarization, and the lensing potential that have the correct correlations between themselves. In these simulations we have assumed no primordial B-mode polarization ( $r = 0$ ), so  $b_{\ell m} = 0$  for each  $\ell$  and  $m$ . For this purpose, we will use a Cholesky decomposition of the covariance matrix of the three fields [17].

We are going to start by defining what a Cholesky decomposition is:

**Theorem 2.1.** *Let  $A \in \mathbb{R}^{n \times n}$ . Then the following conditions are equivalent:*

- a) *A is a symmetric positive-definite matrix.*
- b) *Exists a unique factorization of the form  $A = LL^T$ , where L is a lower triangular matrix. This factorization is called the **Cholesky decomposition** of the matrix A.*

A covariance matrix is always a positive semi-definite matrix, which means that not every time a Cholesky decomposition can be performed. However, in this case, the CMB and lensing potential fields are only partially correlated and the covariance matrix for each  $\ell$  is positive definite. This statement has been checked numerically through the computation of the Cholesky decomposition for all the multipoles. Then, in fact, it is a valid approach to the problem.

The covariance matrix,  $C(\ell)$ , of the three fields is given by

$$C(\ell) = \begin{pmatrix} C_\ell^{TT} & C_\ell^{TE} & C_\ell^{T\phi} \\ C_\ell^{TE} & C_\ell^{EE} & C_\ell^{E\phi} \\ C_\ell^{T\phi} & C_\ell^{E\phi} & C_\ell^{\phi\phi} \end{pmatrix}, \quad (2.1)$$

where the angular power spectra are those from Subsection 2.1.1.

The Cholesky decomposition of the covariance matrix satisfies  $C(\ell) = L(\ell)L^T(\ell)$  where

$$L(\ell) = \begin{pmatrix} L_{11}(\ell) & 0 & 0 \\ L_{21}(\ell) & L_{22}(\ell) & 0 \\ L_{31}(\ell) & L_{32}(\ell) & L_{33}(\ell) \end{pmatrix}, \quad (2.2)$$

and the corresponding elements of the matrix  $L(\ell)$  are

$$\begin{aligned} L_{11}(\ell) &= \sqrt{C_\ell^{TT}}, & L_{21}(\ell) &= \frac{C_\ell^{TE}}{\sqrt{C_\ell^{TT}}}, & L_{31}(\ell) &= \frac{C_\ell^{T\phi}}{\sqrt{C_\ell^{TT}}}, \\ L_{22}(\ell) &= \sqrt{C_\ell^{EE} - \frac{(C_\ell^{TE})^2}{C_\ell^{TT}}}, & L_{32}(\ell) &= \frac{C_\ell^{E\phi} - \frac{C_\ell^{TE}C_\ell^{T\phi}}{C_\ell^{TT}}}{\sqrt{C_\ell^{EE} - \frac{(C_\ell^{TE})^2}{C_\ell^{TT}}}}, \\ L_{33}(\ell) &= \sqrt{C_\ell^{\phi\phi} - \frac{(C_\ell^{T\phi})^2}{C_\ell^{TT}} - \frac{\left(C_\ell^{E\phi} - \frac{C_\ell^{TE}C_\ell^{T\phi}}{C_\ell^{TT}}\right)^2}{C_\ell^{EE} - \frac{(C_\ell^{TE})^2}{C_\ell^{TT}}}}. \end{aligned} \quad (2.3)$$

At this point we know how to compute the Cholesky decomposition of the covariance matrix  $C(\ell)$ . Now, we will generate correlated Gaussian spherical harmonic coefficients for the unlensed temperature,  $t_{\ell m}$ , E-mode polarization,  $e_{\ell m}$ , and lensing potential,  $\phi_{\ell m}$ , using the following equation:

$$\begin{pmatrix} t_{\ell m} \\ e_{\ell m} \\ \phi_{\ell m} \end{pmatrix} = \begin{pmatrix} L_{11}(\ell) & 0 & 0 \\ L_{21}(\ell) & L_{22}(\ell) & 0 \\ L_{31}(\ell) & L_{32}(\ell) & L_{33}(\ell) \end{pmatrix} \begin{pmatrix} h_{\ell m} \\ j_{\ell m} \\ k_{\ell m} \end{pmatrix} \quad (2.4)$$

where  $h_{\ell m}$ ,  $j_{\ell m}$ , and  $k_{\ell m}$  are uncorrelated complex Gaussian variables of zero mean and unit variance [18]. Additionally, as the  $t_{\ell m}$ ,  $e_{\ell m}$ , and  $\phi_{\ell m}$  are the complex harmonic coefficients of a real field,  $h_{\ell m}$ ,  $j_{\ell m}$ , and  $k_{\ell m}$  have to verify the reality condition

$$a_{\ell m}^* = (-1)^m a_{\ell -m}, \quad (2.5)$$

where  $a \in \{h, j, k\}$  [19].

To generate uncorrelated Gaussian spherical harmonic coefficients we have used several functions from the `healpy`<sup>2</sup> package [20], which is a `Python` package based on the Hierarchical Equal Area isoLatitude Pixelation (`HEALPix`<sup>3</sup>) [21] software that has different methods to perform numerical analysis of functions on the sphere. We start with an arbitrary non-zero initial power spectrum. Then, using the function `synalm`, we generate a set of  $a_{\ell m}$  given the power spectrum  $C_\ell$ . Finally, we divide each  $a_{\ell m}$  by the square root of their power spectrum  $C_\ell$ . In our code we have used  $C_\ell = 1$  for  $0 \leq \ell \leq \ell_{max} = 3500$ , so this final step is not necessary. Applying this procedure three times, we generate the three uncorrelated Gaussian spherical harmonic coefficients  $h_{\ell m}$ ,  $j_{\ell m}$ , and  $k_{\ell m}$  of unit variance.

### 2.1.3 Lensing the CMB maps

Weak gravitational lensing deflects CMB photons coming from an original direction  $\hat{\mathbf{n}}'$  on the last scattering surface to an observed direction  $\hat{\mathbf{n}}$ . The two directions are related by the deflection vector,  $\boldsymbol{\alpha}(\hat{\mathbf{n}}) = \nabla\phi(\hat{\mathbf{n}})$ , where the observed lensed CMB field  $\tilde{X}$  is obtained by remapping the corresponding unlensed CMB field  $X \in \{T, Q, U\}$ :

$$\tilde{X}(\hat{\mathbf{n}}) = X(\hat{\mathbf{n}}') = X(\hat{\mathbf{n}} + \boldsymbol{\alpha}(\hat{\mathbf{n}})). \quad (2.6)$$

The typical deviations of the CMB photons are  $\sim 2$  arcmins. For that reason, we will work under the Born approximation. This means that the deflection is considered constant between  $\hat{\mathbf{n}}$  and  $\hat{\mathbf{n}}'$  and the deflection field is evaluated along the unperturbed direction. The practical consequence is that to compute the lensed CMB at a given point it is sufficient to calculate the unlensed CMB at another position in the sky as shown in equation (2.6) [22].

The lensing potential is a scalar function and can be expanded in spherical harmonics. However, the gradient of the lensing potential is a vector field and to make an spherical harmonics transform we have to use a spin-1 basis. Considering the components of  $\nabla\phi(\hat{\mathbf{n}})$

<sup>2</sup>Documentation available at <https://healpy.readthedocs.io/en/latest/>

<sup>3</sup><https://healpix.sourceforge.io/>

with respect to the helicity basis  $\mathbf{e}_\pm \equiv \hat{\mathbf{e}}_\theta \pm i\hat{\mathbf{e}}_\varphi$ ,  $\mathbf{e}_\pm \cdot \nabla\phi(\hat{\mathbf{n}})$ , they can be expanded in spin-1 spherical harmonic functions:

$$\mathbf{e}_\pm \cdot \nabla\phi(\hat{\mathbf{n}}) = \sum_{\ell m} \pm 1 a_{\ell m} \pm 1 Y_{\ell m}(\hat{\mathbf{n}}), \quad (2.7)$$

where

$$\begin{aligned} {}_1a_{\ell m} &= \int d\Omega (\mathbf{e}_+ \cdot \nabla\phi(\hat{\mathbf{n}})) {}_1Y_{\ell m}^*(\hat{\mathbf{n}}) = - \int d\Omega \bar{\partial}\phi(\hat{\mathbf{n}}) {}_1Y_{\ell m}^*(\hat{\mathbf{n}}) \\ &= - \int d\Omega \sum_{\ell' m'} \phi_{\ell' m'} \sqrt{\ell'(\ell'+1)} {}_1Y_{\ell' m'}(\hat{\mathbf{n}}) {}_1Y_{\ell m}^*(\hat{\mathbf{n}}) = -\sqrt{\ell(\ell+1)}\phi_{\ell m}, \\ {}_{-1}a_{\ell m} &= \int d\Omega (\mathbf{e}_- \cdot \nabla\phi(\hat{\mathbf{n}})) {}_{-1}Y_{\ell m}^*(\hat{\mathbf{n}}) = - \int d\Omega \bar{\partial}^*\phi(\hat{\mathbf{n}}) {}_{-1}Y_{\ell m}^*(\hat{\mathbf{n}}) \\ &= \int d\Omega \sum_{\ell' m'} \phi_{\ell' m'} \sqrt{\ell'(\ell'+1)} {}_{-1}Y_{\ell' m'}(\hat{\mathbf{n}}) {}_{-1}Y_{\ell m}^*(\hat{\mathbf{n}}) = \sqrt{\ell(\ell+1)}\phi_{\ell m}, \end{aligned} \quad (2.8)$$

in which  $\bar{\partial}$  is the spin raising operator and we have applied that

$$\phi(\hat{\mathbf{n}}) = \sum_{\ell m} \phi_{\ell m} Y_{\ell m}(\hat{\mathbf{n}}), \quad \int d\Omega {}_s Y_{\ell m}(\hat{\mathbf{n}}) {}_s Y_{\ell' m'}^*(\hat{\mathbf{n}}) = \delta_{\ell\ell'} \delta_{mm'}. \quad (2.9)$$

The deflection field could be now easily calculated from

$$\mathbf{e}_+ \cdot \nabla\phi(\hat{\mathbf{n}}) = (\nabla\phi(\hat{\mathbf{n}}))_\theta + i(\nabla\phi(\hat{\mathbf{n}}))_\varphi, \quad (2.10)$$

where the real and the imaginary part correspond to the  $\hat{\mathbf{e}}_\theta$  and  $\hat{\mathbf{e}}_\varphi$  components of the deflection field,  $\nabla\phi(\hat{\mathbf{n}})$ , respectively.

Defining  $\beta$  as the angle between the deflection vector,  $\boldsymbol{\alpha}(\hat{\mathbf{n}}) = \nabla\phi(\hat{\mathbf{n}})$ , and  $\hat{\mathbf{e}}_\theta$ , such that

$$\boldsymbol{\alpha}(\hat{\mathbf{n}}) = \alpha \cos \beta \hat{\mathbf{e}}_\theta + \alpha \sin \beta \hat{\mathbf{e}}_\varphi, \quad (2.11)$$

where  $\alpha = |\boldsymbol{\alpha}(\hat{\mathbf{n}})|$ , and the value of a lensed field  $\tilde{X}$  in a direction  $\hat{\mathbf{n}} = (\theta, \varphi)$  is given by the unlensed field  $X \in \{T, Q, U\}$  at  $\hat{\mathbf{n}}' = (\theta', \varphi + \Delta\varphi)$  where

$$\begin{aligned} \cos \theta' &= \cos \alpha \cos \theta - \sin \alpha \sin \theta \cos \beta, \\ \sin \Delta\varphi &= \frac{\sin \alpha \sin \beta}{\sin \theta'}. \end{aligned} \quad (2.12)$$

The previous equations have been derived using identities for spherical triangles. This approach is very accurate in general except near the coordinate singularities.

For polarization, which is a spin-2 field, we need to account for the different directions of the coordinate vectors at the two points  $\hat{\mathbf{n}}$  and  $\hat{\mathbf{n}}'$ . This requires rotating the components of the spherical polar coordinates by an angle  $\gamma = \beta - \beta'$ , which is the difference between the angle made by  $\hat{\mathbf{e}}_\theta$  and the geodesic connecting the two points. This is done by multiplying the unlensed polarization field by an extra factor to obtain the corresponding lensed field [23]:

$$(\tilde{Q} + i\tilde{U})(\hat{\mathbf{n}}) = e^{2i\gamma}(\tilde{Q} + i\tilde{U})(\hat{\mathbf{n}}'), \quad (2.13)$$

where, again,  $\hat{\mathbf{n}} = (\theta, \varphi)$  and  $\hat{\mathbf{n}}' = (\theta', \varphi + \Delta\varphi)$ , and the angle  $\gamma$  can be calculated using the following equation:

$$\gamma = \beta - \beta' = \beta - \arctan\left(\frac{\alpha \sin \beta}{\alpha \sin \alpha \cot \theta + \alpha \cos \beta \cos \alpha}\right), \quad (2.14)$$

where

$$\beta = \arctan\left(\frac{(\nabla\phi(\hat{\mathbf{n}}))_\varphi}{(\nabla\phi(\hat{\mathbf{n}}))_\theta}\right). \quad (2.15)$$

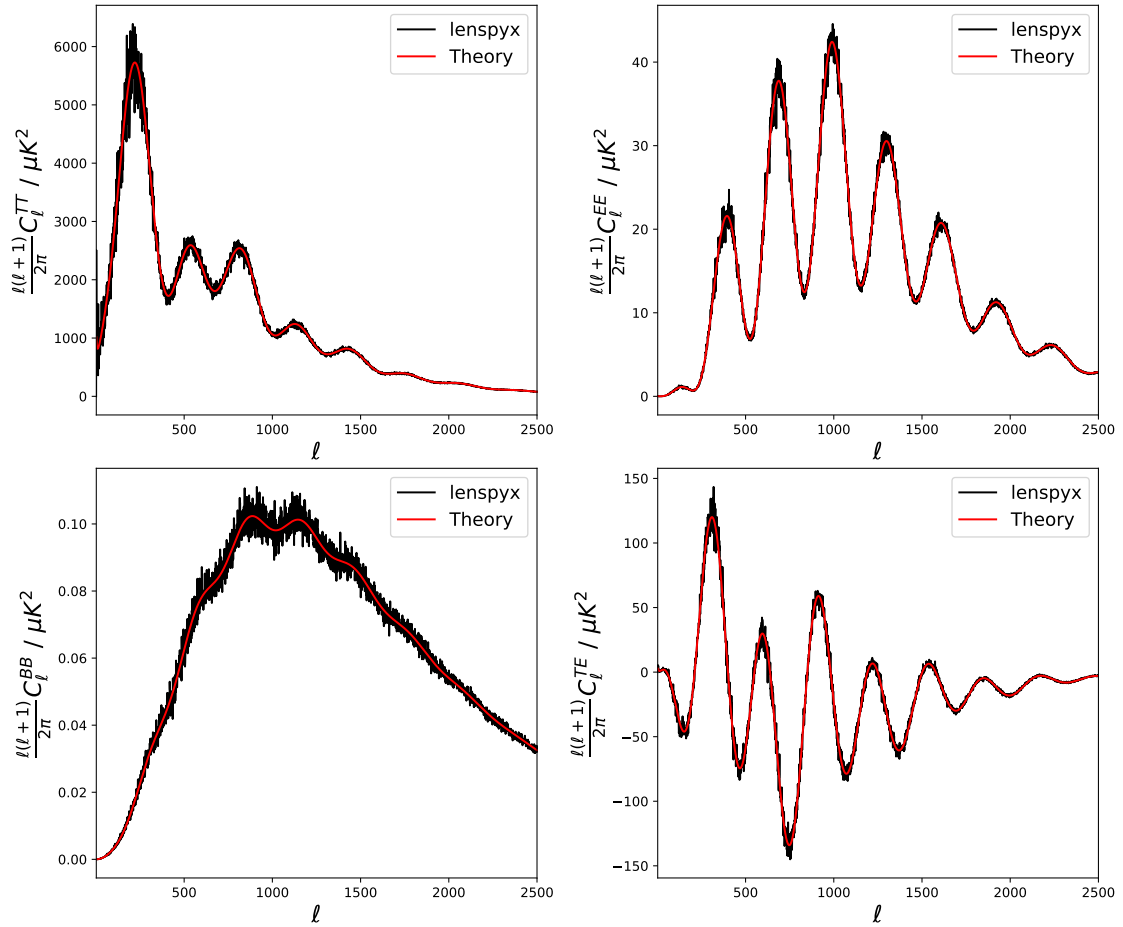


Figure 2.3: The recovered angular power spectra from the lensed  $T$ ,  $Q$  and  $U$  maps compared with the lensed angular power spectra computed with CLASS using Planck 2018  $TT, TE, EE + \text{lowE} + \text{lensing}$  cosmological parameters.

All the theory needed to compute simulated lensed CMB maps has already been presented. However, we have to face certain computational limitations connected with the fact that we are working with discrete maps. Given a unlensed pixelated CMB map,  $X$ , we want to compute its value at a position  $\hat{\mathbf{n}}' = \hat{\mathbf{n}} + \boldsymbol{\alpha}(\hat{\mathbf{n}})$ , which, in general, will not correspond to a pixel center on the map. The calculation could still be done, but at a

higher computational cost, because it requires computing

$$X(\hat{\mathbf{n}} + \boldsymbol{\alpha}(\hat{\mathbf{n}})) = \sum_{\ell m} a_{\ell m} Y_{\ell m}(\hat{\mathbf{n}} + \boldsymbol{\alpha}(\hat{\mathbf{n}})). \quad (2.16)$$

The calculation of the previous equation is just for one pixel. For the full map, it would take  $O(N_{pix}^2)$  operations, which is a prohibitive cost for the high resolution maps we are working with. The solution is to use interpolation with neighbouring pixels in the computation of  $X(\hat{\mathbf{n}} + \boldsymbol{\alpha}(\hat{\mathbf{n}}))$ .

At this point, we have all the necessary tools to calculate the lensed maps. We are going to lens the CMB maps using a software called `lenspyx`, which is a curved-sky Python lensed CMB maps simulation package developed by Julien Carron. It is strongly based on the software `LensPix`, written in `Fortran` and developed by Anthony Lewis. The software `lenspyx` uses a bicubic interpolation in a oversampled grid and, instead of using the typical `HEALPix` pixelization, `lenspyx` uses an Equidistant Cylindrical Projection of the sphere (ECP), which has been proven to be computationally cheaper [24, 25].

Given unlensed  $(T, Q, U) + \phi$  maps from the  $(t_{\ell m}, e_{\ell m}, b_{\ell m} = 0, \phi_{\ell m})$  harmonic coefficients, we lens the maps using the functions `alm2lenmap` and `alm2lenmap_spin` for the temperature and the polarization maps, respectively. The lensed maps  $(\tilde{T}, \tilde{Q}, \tilde{U})$  have a resolution of  $N_{side} = 2048$ , corresponding to  $N_{pix} \approx 5 \cdot 10^7$  rhomboid pixels with a 1.72 arcmins side. The lensed maps are constructed by remapping the unlensed ones, after having interpolated them at a resolution of approximately 0.35 arcmins.

## 2.2 Observed CMB maps by different experiments

In this Section we consider an idealized experiment  $M$  that is only affected by limited angular resolution, instrumental noise, and partial sky coverage. After explaining how the observed signal is affected by the previous effects, in Subsection 2.2.1 we briefly describe *Planck* and LiteBird experiments, in Subsection 2.2.2 we explain how the combination of the two experiments is done and, finally, in Subsection 2.2.3, we show how to deal with partial sky coverage.

First, the limited angular resolution is modelled by smoothing the lensed CMB  $(\tilde{T}, \tilde{Q}, \tilde{U})$  maps with a Gaussian symmetric beam. In harmonic space, this smoothing is given by a beam function  $b_{\ell, XY}^M$ , using the `healpy` function `smoothing`. Then, we simulate a realization of instrumental noise in which the noise in each pixel is Gaussian and uncorrelated with the noise in any other pixel and with the cosmological signal. This noise map is generated by sampling from a normal distribution  $\mathcal{N}(0, \sigma_{pix, X}^M)$  and added to the smoothed  $(\tilde{T}, \tilde{Q}, \tilde{U})$  maps. When working in harmonic space, the instrumental noise introduces an additive term,  $N_{\ell}^{XY, M}$ , as shown in the following equation:

$$C_{\ell}^{XY, M} = b_{\ell, XY}^M{}^2 C_{\ell}^{XY} + N_{\ell}^{XY, M}, \quad (2.17)$$

where  $X, Y \in \{T, E, B\}$ ,  $M \in \{P, L, C\}$  is the experiment under consideration and can be either *Planck* ( $P$ ), LiteBIRD ( $L$ ) or the combination of them ( $C$ ), and  $C_{\ell}^{XY}$  corresponds to the  $XY$  theoretical angular power spectrum. The beam function depends on the FWHM<sup>4</sup>

<sup>4</sup>FWHM and standard deviation,  $\sigma$ , are easily related by  $\sigma = \text{FWHM}/\sqrt{8 \ln 2}$ .

of the beam,  $\sigma_B^M$ , and slightly on the spin  $s$  of the field [26],

$$b_{\ell,XY} = \exp([- \ell(\ell + 1)/2 + s]\sigma_B^{M^2}), \quad (2.18)$$

where  $s = 0$  for TT,  $s = 1$  for TE and  $s = 2$  for EE and BB.

The instrumental noise is given by

$$N_{\ell}^{XY,M} = \begin{cases} \frac{4\pi\sigma_{pix,X}^M{}^2}{N_{pix}}, & \text{if } X = Y \\ 0, & \text{if } X \neq Y \end{cases} \quad (2.19)$$

where  $\sigma_{pix,X}^M$  is the noise per pixel for the  $X$  map and  $N_{pix}$  is the number of pixels of the map. Note that for  $X \neq Y$ , the noise is zero because the random noise realizations are not correlated with each other.

At this point, it is interesting to deconvolve the effects of the beam to obtain an estimate of  $C_{\ell}^{XY,M}$  as close as possible to  $C_{\ell}^{XY}$ :

$$C_{\ell}^{XY,M'} = \frac{C_{\ell}^{XY,M}}{b_{\ell,XY}^M{}^2} = C_{\ell}^{XY} + \frac{N_{\ell}^{XY,M}}{b_{\ell,XY}^M{}^2}. \quad (2.20)$$

After doing this, the constant noise power spectrum that we have in equation (2.19) explodes at high  $\ell$  due to the dominant contribution of  $b_{\ell,XY}^M$ .

### 2.2.1 *Planck* and LiteBIRD experiments

The *Planck* satellite was a European mission that ended on 2013. It observed the CMB using an array of 74 detectors to measure the sky in nine bands, covering frequencies between 25 and 1000 GHz, with angular resolutions between 33 and 5 arcmins. Our simulations take as reference the noise level of a typical clean CMB map. This leads to a noise per pixel for temperature of  $\sigma_{pix,T}^P = 20 \mu\text{K}\cdot\text{arcmin}$  and for polarization  $\sigma_{pix,E}^P = \sigma_{pix,B}^P = 40 \mu\text{K}\cdot\text{arcmin}$ , and an effective circular Gaussian beam with a FWHM of 5 arcmins [27].

LiteBIRD is JAXA's CMB space mission for the study of B-mode polarization and Inflation. JAXA, the Japanese Space Agency, selected LiteBIRD in May 2019 as a strategic large-class (L-class) mission, with its expected launch date in the late 2020s. LiteBIRD will use 15 frequency bands between 34 and 448 GHz to achieve a total polarization sensitivity of  $\sigma_{pix,E}^L = \sigma_{pix,B}^L = 2.2 \mu\text{K}\cdot\text{arcmin}$ . In this project we will also consider this noise value for temperature  $\sigma_{pix,T}^L$ . The typical angular resolution of LiteBIRD is a FWHM of 30 arcmin at 100 GHz [28].

Using the experimental characteristics of both experiments, and considering the procedure explained at the beginning of Section 2.2, we generate simulations of the observed CMB maps by *Planck*,  $(\tilde{T}, \tilde{Q}, \tilde{U})_{\text{Planck}}$ , and LiteBIRD,  $(\tilde{T}, \tilde{Q}, \tilde{U})_{\text{LiteBIRD}}$ . As it will be needed in the forthcoming Sections, we compute the harmonic coefficients from the CMB maps for *Planck*,  $(t_{\ell m}^P, e_{\ell m}^P, b_{\ell m}^P)$ , and for LiteBIRD,  $(t_{\ell m}^L, e_{\ell m}^L, b_{\ell m}^L)$ , using the `healpy` function `map2alm`.

## 2.2. OBSERVED CMB MAPS BY DIFFERENT EXPERIMENTS

In Figure 2.4, we can observe expected data from LiteBIRD, and measurements from other CMB experiments. *Planck* has measured temperature to an exquisite precision, thanks to its low instrumental noise levels. LiteBIRD promises to do the same for polarization, although only for the largest scales due to its limited angular resolution. Here exquisite precision refers to the limit imposed by the cosmic variance in temperature. LiteBIRD is expected to reach that limit for the E-mode polarization. Consequently, *Planck* and LiteBIRD are two complementary experiments because *Planck* provides precise temperature and small scale information and LiteBIRD will provide precise polarization information. For that reason, we combine both experiments in Subsection 2.2.2 to quantify how beneficial it would be for the lensing reconstruction.

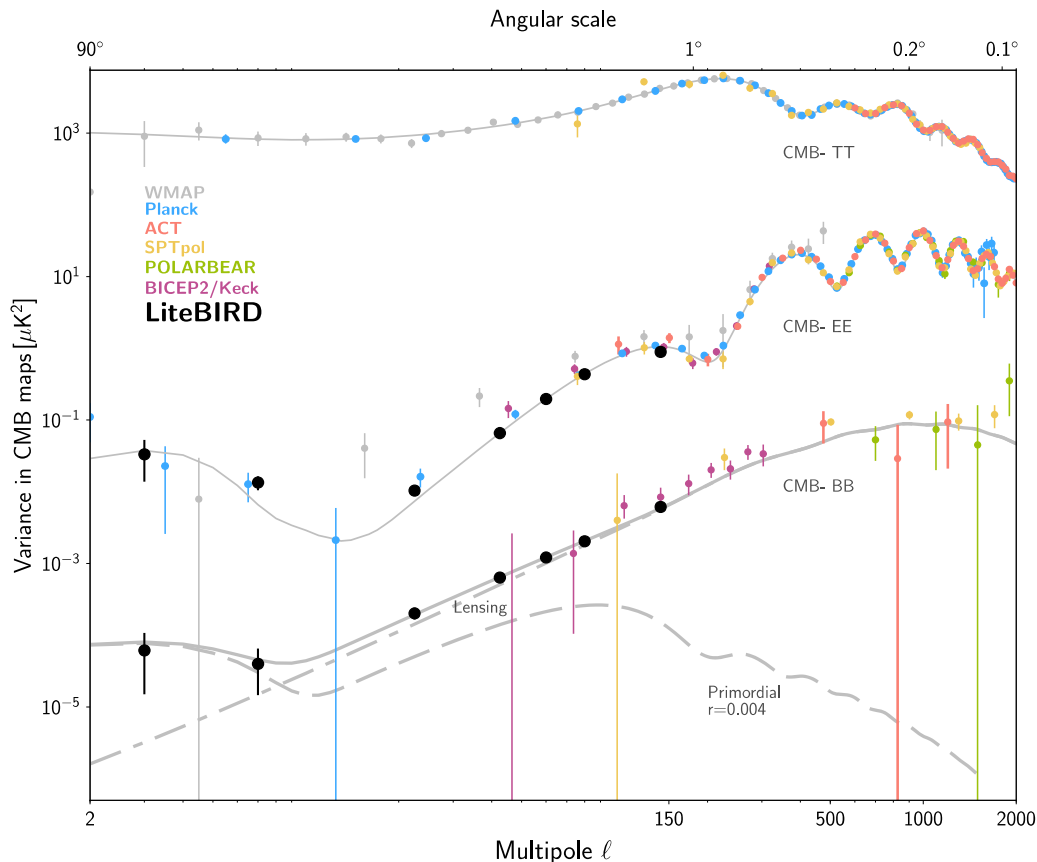


Figure 2.4: Summary of present measurements of CMB power spectra and expected polarization sensitivity of LiteBIRD. Figure from [28].

### 2.2.2 Combination of *Planck* and LiteBIRD experiments

This is one of the crucial parts of this work and related to the title of this document. Here we develop a procedure to combine *Planck* and LiteBIRD data given CMB maps of both experiments.

Given the harmonic coefficients from the CMB maps for *Planck*,  $(t_{\ell m}^P, e_{\ell m}^P, b_{\ell m}^P)$ , and

## 2.2. OBSERVED CMB MAPS BY DIFFERENT EXPERIMENTS

for LiteBIRD,  $(t_{\ell m}^L, e_{\ell m}^L, b_{\ell m}^L)$ , we can combine them to produce  $(t_{\ell m}^C, e_{\ell m}^C, b_{\ell m}^C)$  using a weighted sum:

$$\begin{aligned} t_{\ell m}^C &= w_{\ell}^{P,T} t_{\ell m}^P + w_{\ell}^{L,T} t_{\ell m}^L, \\ e_{\ell m}^C &= w_{\ell}^{P,E} e_{\ell m}^P + w_{\ell}^{L,E} e_{\ell m}^L, \\ b_{\ell m}^C &= w_{\ell}^{P,B} b_{\ell m}^P + w_{\ell}^{L,B} b_{\ell m}^L, \end{aligned} \quad (2.21)$$

where the weights are  $w_{\ell}^{M,Y}$  for  $M \in \{P, L\}$  and  $Y \in \{T, E, B\}$  and verify

$$w_{\ell}^{P,Y} + w_{\ell}^{L,Y} = 1, \quad w_{\ell}^{M,Y} \propto \frac{1}{N_{\ell}^{YY,M} b_{\ell,YY}^M{}^{-2}}, \quad (2.22)$$

leading to the following equations:

$$w_{\ell}^{P,Y} = \frac{N_{\ell}^{YY,L} b_{\ell,YY}^L{}^{-2}}{N_{\ell}^{YY,P} b_{\ell,YY}^P{}^{-2} + N_{\ell}^{YY,L} b_{\ell,YY}^L{}^{-2}}, \quad w_{\ell}^{L,Y} = \frac{N_{\ell}^{YY,P} b_{\ell,YY}^P{}^{-2}}{N_{\ell}^{YY,P} b_{\ell,YY}^P{}^{-2} + N_{\ell}^{YY,L} b_{\ell,YY}^L{}^{-2}}. \quad (2.23)$$

The weights that appear in equation (2.22) are inversely proportional to the noise term of equation (2.20). Thus, we are performing an inverse-variance weighting, minimizing the variance of the combination and favouring the experiment with the smallest noise term. In Figure 2.5, the weights are plotted for the *Planck* and LiteBIRD experiments. As it can be concluded from this Figure, LiteBIRD is the dominant contribution at the low  $\ell$  region ( $\ell < 600$ ) and *Planck* dominates at the high  $\ell$  region ( $\ell > 600$ ). The reasons behind that are the low instrumental noise and resolution of the LiteBIRD mission in contrast to the *Planck* experiment.

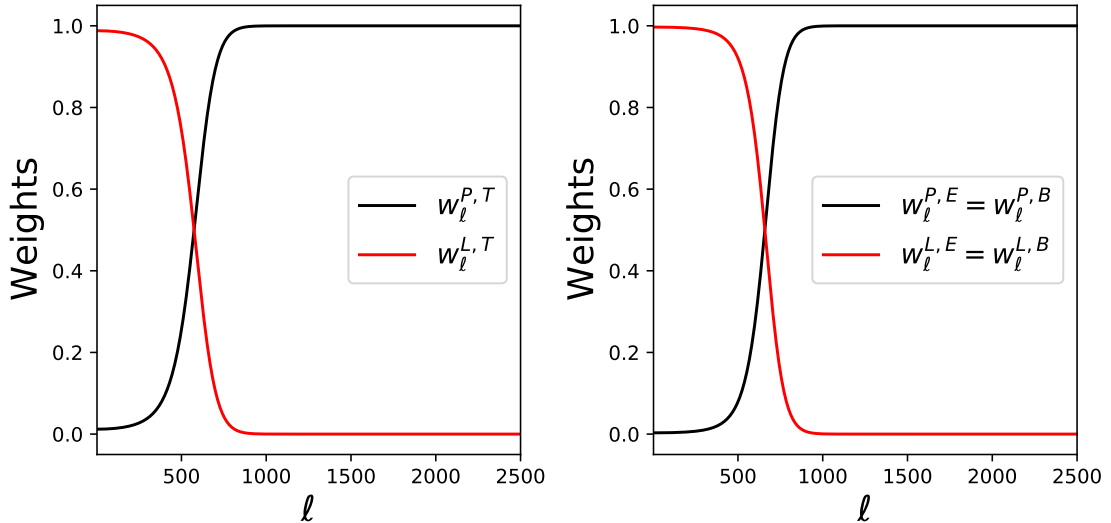


Figure 2.5: Plots of the weights for *Planck* and LiteBIRD experiments for the  $t_{\ell m}$ ,  $e_{\ell m}$  and  $b_{\ell m}$  harmonic coefficients. The left figure correspond to the temperature weights and the right figure to the polarization weights.

Using equation (2.21) we can calculate the beam and instrumental noise for the combination of *Planck* and LiteBIRD experiments. Let start by computing the temperature angular power spectrum

$$C_\ell^{TT,C} = \frac{1}{2\ell+1} \sum_{m=-\ell}^{\ell} |t_{\ell m}^C|^2 = (w_\ell^{P,T})^2 C_\ell^{TT,P} + (w_\ell^{L,T})^2 C_\ell^{TT,L} + \frac{2w_\ell^{P,T} w_\ell^{L,T}}{2\ell+1} \sum_{m=-\ell}^{\ell} \text{Re}\{t_{\ell m}^{P*} t_{\ell m}^L\}, \quad (2.24)$$

where

$$\begin{aligned} C_\ell^{TT,P} &= b_{\ell,TT}^P{}^2 C_\ell^{TT} + N_\ell^{TT,P}, \\ C_\ell^{TT,L} &= b_{\ell,TT}^L{}^2 C_\ell^{TT} + N_\ell^{TT,L}. \end{aligned} \quad (2.25)$$

To calculate the cross-term of equation (2.24) we use

$$\begin{aligned} t_{\ell m}^P &= \tilde{t}_{\ell m} b_{\ell,TT}^P + n_{\ell m}^{TT,P}, \\ t_{\ell m}^L &= \tilde{t}_{\ell m} b_{\ell,TT}^L + n_{\ell m}^{TT,L}, \end{aligned} \quad (2.26)$$

where  $\tilde{t}_{\ell m}$  are the temperature spherical harmonics coefficients of the signal,  $N_\ell^{TT,P} = \langle n_{\ell m}^{TT,P} n_{\ell m}^{TT,P*} \rangle$  and  $N_\ell^{TT,L} = \langle n_{\ell m}^{TT,L} n_{\ell m}^{TT,L*} \rangle$ . Then,

$$t_{\ell m}^{P*} t_{\ell m}^L = b_{\ell,TT}^P b_{\ell,TT}^L |\tilde{t}_{\ell m}|^2 + \text{noise terms}, \quad (2.27)$$

where the noise terms vanish when performing the summation because they are not correlated, so they are not shown. Finally,

$$\frac{2w_\ell^{P,T} w_\ell^{L,T}}{2\ell+1} \sum_{m=-\ell}^{\ell} \text{Re}\{t_{\ell m}^{P*} t_{\ell m}^L\} = 2w_\ell^{P,T} w_\ell^{L,T} b_{\ell,TT}^P b_{\ell,TT}^L C_\ell^{TT}, \quad (2.28)$$

and substituting in equation (2.24) we get

$$C_\ell^{TT,C} = b_{\ell,TT}^C{}^2 C_\ell^{TT} + N_\ell^{TT,C}, \quad (2.29)$$

where

$$\begin{aligned} b_{\ell,TT}^C{}^2 &= \left(w_\ell^{P,T} b_{\ell,TT}^P\right)^2 + \left(w_\ell^{L,T} b_{\ell,TT}^L\right)^2 + 2w_\ell^{P,T} w_\ell^{L,T} b_{\ell,TT}^P b_{\ell,TT}^L, \\ N_\ell^{TT,C} &= \left(w_\ell^{P,T}\right)^2 N_\ell^{TT,P} + \left(w_\ell^{L,T}\right)^2 N_\ell^{TT,L}. \end{aligned} \quad (2.30)$$

The same expression is obtained for  $C_\ell^{EE,C}$  and  $C_\ell^{BB,C}$  just changing the beam, noise, and weights for polarization.

The cross-correlation between temperature and E-mode polarization for the combination can also be computed in a similar manner:

$$\begin{aligned} C_\ell^{TE} &= \frac{1}{2\ell+1} \sum_{m=-\ell}^{\ell} t_{\ell m}^C{}^* e_{\ell m}^C = w_\ell^{P,T} w_\ell^{P,E} C_\ell^{TE,P} + w_\ell^{L,T} w_\ell^{L,E} C_\ell^{TE,L} \\ &\quad + \frac{w_\ell^{P,T} w_\ell^{L,E}}{2\ell+1} \sum_{m=-\ell}^{\ell} t_{\ell m}^{P*} e_{\ell m}^L + \frac{w_\ell^{P,E} w_\ell^{L,T}}{2\ell+1} \sum_{m=-\ell}^{\ell} t_{\ell m}^{L*} e_{\ell m}^P, \end{aligned} \quad (2.31)$$

## 2.2. OBSERVED CMB MAPS BY DIFFERENT EXPERIMENTS

where

$$\begin{aligned} C_\ell^{TE,P} &= b_{\ell,TE}^P{}^2 C_\ell^{TE}, \\ C_\ell^{TE,L} &= b_{\ell,TE}^L{}^2 C_\ell^{TE}. \end{aligned} \quad (2.32)$$

Following a similar procedure to temperature, from equation (2.31) we get

$$C_\ell^{TE,C} = b_{\ell,TE}^C{}^2 C_\ell^{TE}, \quad (2.33)$$

$$\begin{aligned} b_{\ell,TE}^C{}^2 &= w_\ell^{P,T} w_\ell^{P,E} (b_{\ell,TE}^P)^2 + w_\ell^{L,T} w_\ell^{L,E} (b_{\ell,TE}^L)^2 \\ &+ w_\ell^{P,T} w_\ell^{L,E} b_{\ell,TT}^P b_{\ell,EE}^L + w_\ell^{L,T} w_\ell^{P,E} b_{\ell,TT}^L b_{\ell,EE}^P, \end{aligned} \quad (2.34)$$

In Figures 2.6 and 2.7, the plots of the beam and noise for *Planck*, *LiteBIRD*, and the combination of both experiments are plotted.

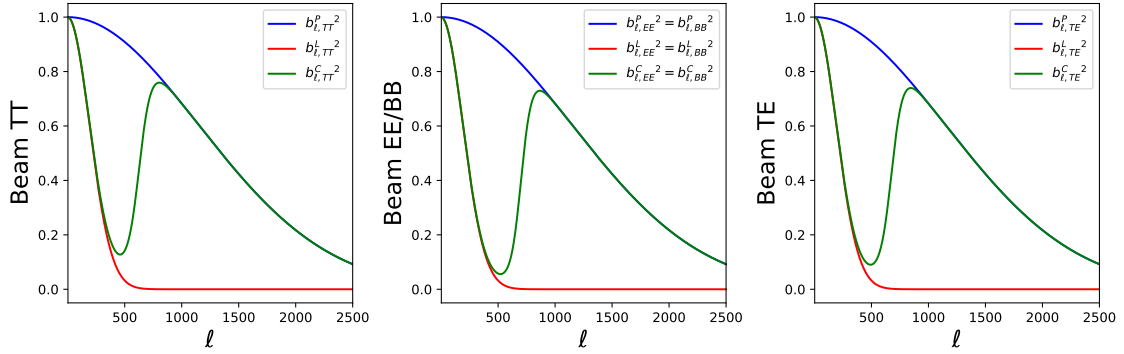


Figure 2.6: Plots of the beam for *Planck*, *LiteBIRD*, and the combination of both experiment for the different angular power spectra.

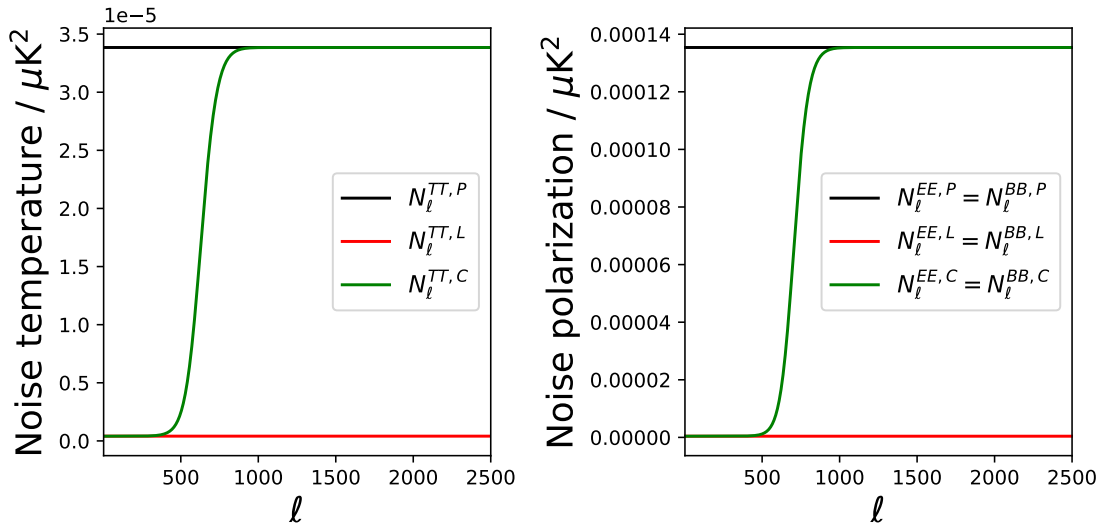


Figure 2.7: Plots of the instrumental noise for *Planck*, *LiteBIRD*, and the combination of both experiment for the different angular power spectra.

## 2.2. OBSERVED CMB MAPS BY DIFFERENT EXPERIMENTS

Figure 2.8 shows the deconvolved angular power spectra of the simulated CMB maps of *Planck*, LiteBIRD, and the combination of them. The deconvolution is just a division by the squared of the beam function. From them, we can observe that LiteBIRD does not contribute too much to the TT and TE angular power spectra, but makes a huge difference in the polarization E and B modes at low  $\ell$ . Especially, the lensed B modes are not detected by *Planck*, but they will be detected by LiteBIRD. As pointed before, the way the combination of *Planck* and LiteBIRD is defined means that we are taking the best experiment for each multipole  $\ell$ .

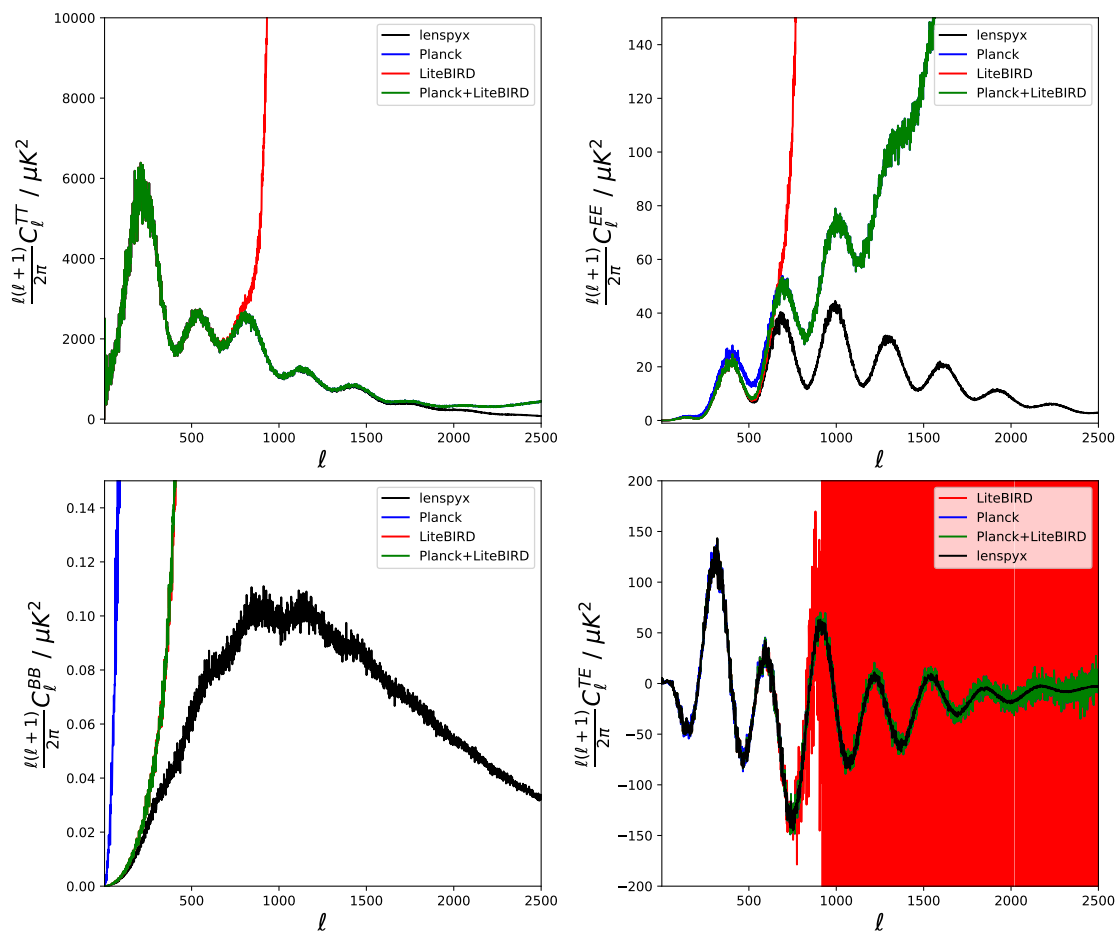


Figure 2.8: Plots of the deconvolved angular power spectra comparing the results from ideal case, *Planck*, *LiteBIRD*, and the combination of *Planck* and *LiteBIRD*.

### 2.2.3 Masking the CMB maps

Masking could be defined as the process of hiding patches of the sky whose microwave emission correspond to other sources distinct from the CMB. In this Section we distinguish between two masks: the point source mask and the Galactic mask.

The point source mask includes all the extragalactic sources emitting in the microwave range, like galaxy clusters, dusty galaxies, or radio-loud active galactic nuclei. They are

compact and isolated objects in the sky. The point mask will not be included in this project because it requires using a technique named inpainting, which consists in restoring a (fake) signal in the contaminated regions. The source holes are filled with a Gaussian realization constrained by the signal around the masked region. As a consequence, some noise is added in a small area of the sky. In [13] the authors have shown that this approach is harmless for lensing, allowing an excellent reconstruction of the power spectrum of the lensing potential without the creation of any spurious lensing signal. Recently the topic has increased in popularity and some problems have been detected. Masking the point sources might be dangerous because they are part of the gravitational potential responsible of lensing and their emission is as well lensed by the large scale structure between them and us. This could lead to correlations and biases [29]. This will be part of extensive work in the future.

The second group corresponds to the Galactic mask, which basically covers the Galactic plane of the CMB map to hide the Milky Way's microwave emission. Masking produces two major impacts on the recovered angular power spectrum, which are a considerable reduction on the amplitude of the signal related to the percentage of the sky covered by the mask, and a coupling between different multipoles, modelled by the coupling matrix presented in Subsection 1.2.3. Additionally, related to the use of lensing quadratic estimators, masking introduces a mask mean field bias which occurs even in the absence of lensing and must be removed. The quadratic estimators exploits the correlations between multipoles and by masking we are introducing artificial correlations.

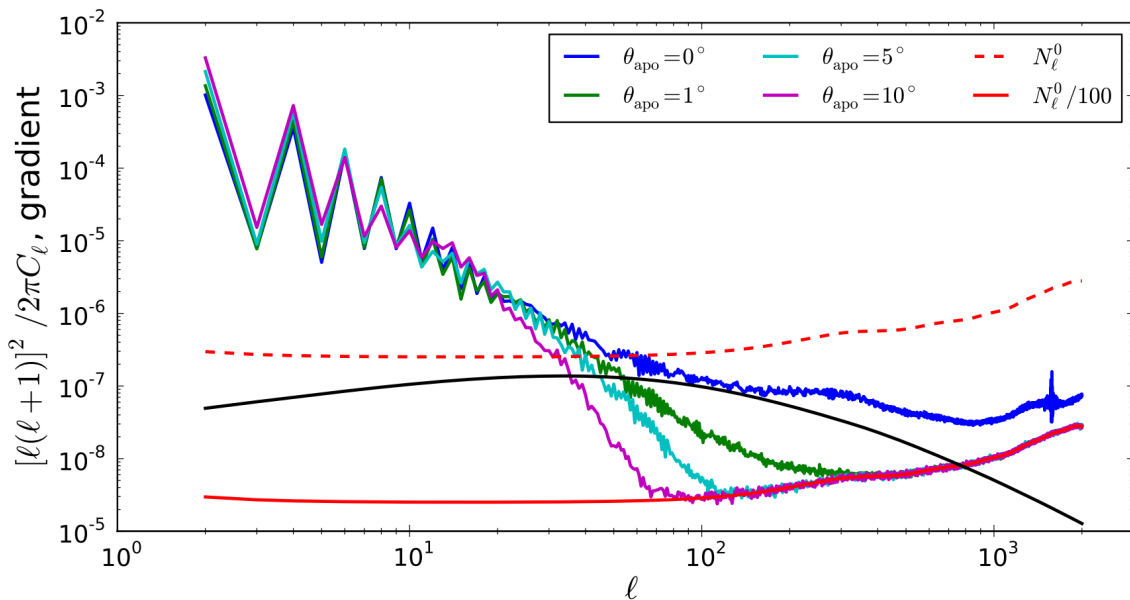


Figure 2.9: Power spectrum of the mask mean field rescaled by  $f_{gal,A}$ . When the binary Galactic mask is applied (blue lines) the reconstruction is strongly biased at high multipoles. Figure from [13].

## 2.2. OBSERVED CMB MAPS BY DIFFERENT EXPERIMENTS

To minimize the last two effects produced by masking, we are going to use a technique called apodization. It consists in a smoothing of the mask using a sin-like function so that the mask border does not go abruptly from 0 to 1. The apodization scale is set to  $10^\circ$  because it reduces the mask mean field bias, as discussed in [13] and shown in Figure 2.9. As it is well known in CMB science, apodization transforms the coupling matrix into an almost diagonal matrix, reducing the off-diagonal terms, and therefore the correlations between different multipoles.

Even though the mask mean field bias has been significantly reduced, it must still be estimated. Although we are not going to estimate this bias in this document, we will explain how it should be taken into account. Simulating  $N_{unl}^{MF}$  simulations of unlensed CMB maps and using a Monte-Carlo procedure, the mask mean field bias is estimated using the following equation:

$$\hat{\phi}_{\ell m}^{MF} = \frac{1}{N_{unl}^{MF}} \sum_{i=1}^{N_{unl}^{MF}} \hat{\phi}_{\ell m}^i. \quad (2.35)$$

In this work we have used the same Galactic mask for both temperature and polarization, corresponding to the 2015 Galactic plane mask GAL080<sup>5</sup> where 80% of the sky has been left unmasked (Figure 2.10). This mask has been used in the analysis of the *Planck* data. After performing a  $10^\circ$  apodization C1 of the mask (Figure 2.11), we multiply it by the lensed  $(\tilde{T}, \tilde{Q}, \tilde{U})$  simulated maps of the different experiments. To apodize the mask we have used `pymaster`<sup>6</sup> [30], which is the Python implementation of the `NaMaster` library.

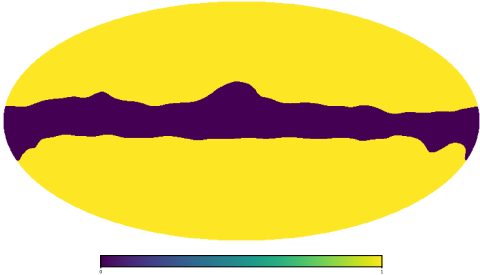


Figure 2.10: 2015 Galactic plane binary mask GAL080 obtained from the Planck Legacy Archive.

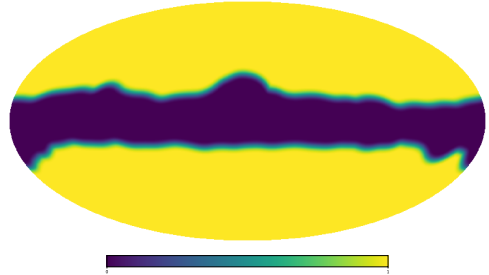


Figure 2.11: 2015 Galactic plane mask GAL080 obtained from the Planck Legacy Archive and apodized with apodization type C1 and a scale of  $10^\circ$  using `pymaster`.

For the 2015 Galactic plane mask GAL080, we have checked the diagonalization of the coupling matrix. Figure 2.12 clearly shows how apodizing the mask with a scale of  $10^\circ$  reduces the off-diagonal terms about six orders of magnitude.

<sup>5</sup>File `HFI_Mask_GalPlane-apo0_2048.R2.00.fits` which can be found in `Maps>Masks>Galactic Plane` in <https://pla.esac.esa.int/#home>

<sup>6</sup><https://namaster.readthedocs.io/en/latest/>

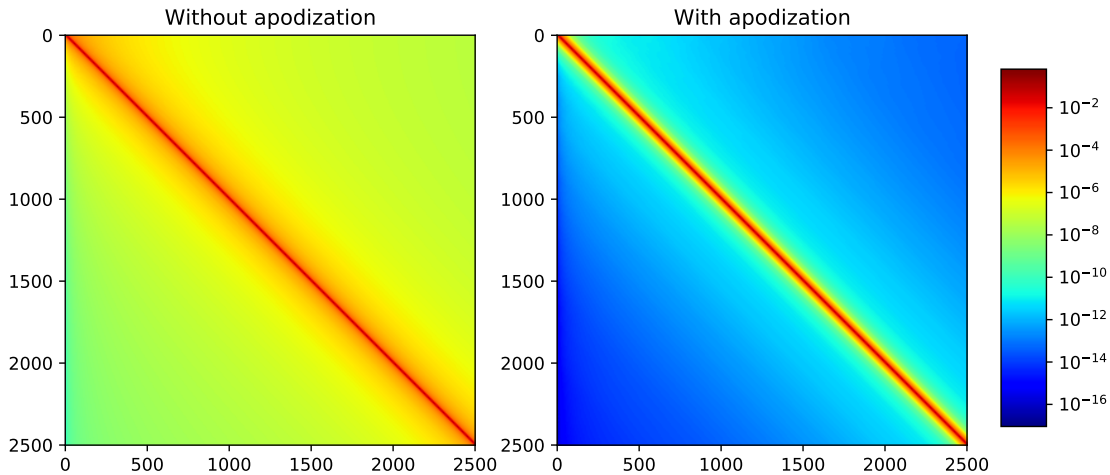


Figure 2.12:  $TT$  coupling matrix of the 2015 Galactic plane mask *GAL080* with and without an apodization of  $10^\circ$  calculated using *pymaster*.

## 2.3 Reconstruction of the lensing potential

For the reconstruction of the lensing potential we are going to use the software `lensQUEST`<sup>7</sup> developed by Dominic Beck. It contains an implementation of the quadratic estimators for lensing reconstruction and the minimum-variance estimator following the equations appearing in [1] and explained in detail in Sections 1.2 and 1.2.2.

To compute the quadratic estimator  $\hat{\phi}_{\ell m}/A_\ell$ , where  $A_\ell$  is the normalization factor, requires the CMB maps in terms of the harmonic coefficients normalized by their angular power spectra ( $t_{\ell m}/\hat{C}_\ell^{TT}, e_{\ell m}/\hat{C}_\ell^{EE}, b_{\ell m}/\hat{C}_\ell^{BB}$ ), the theoretical lensed angular power spectra, and the observed angular power spectra, i.e., as expressed in equation (2.20).

The same approach could be applied for partial sky coverage maps. First, we need to include the effect of the mask in the CMB maps by multiplying them by the apodized mask and recovering the harmonic coefficients of the result. Secondly, we need to take into account how the theoretical and observed angular power spectra change when applying a mask. The approach that we are following is a proposal based on [13]. To do so, we need to calculate the pseudo power spectrum  $\tilde{C}_\ell$  using the mode-mode coupling matrix,  $M_{\ell\ell'}$ :

$$\tilde{C}_\ell = \sum_{\ell'} M_{\ell\ell'} C_{\ell'}, \quad (2.36)$$

where  $C_{\ell'}$  corresponds to a full-sky angular power spectrum [31]. For the computation of the coupling matrix we have used `pymaster` (*NaMaster* library).

The results obtained from the lensing reconstruction are shown and explained in Chapter 3.

<sup>7</sup><https://github.com/doicbek/lensquest>

## 2.4 Wiener filter

In this work, we have considered three different sets of data: *Planck*, LiteBIRD, and the combination of both experiments. Considering we have an observation  $d$  from one of the experiments, it can be decomposed in the sum of a signal,  $s$ , and a noise,  $n$ , as it has been shown in equation (2.20). Assuming both terms are Gaussian and isotropic, we are interested on getting an estimation  $\hat{s}$  of the signal from a noisy observation. One way to proceed, and a very common approach in CMB science, is to apply a Wiener filter to the data, which is the linear filter that minimises the variance of the reconstruction error. Given the harmonic coefficients  $d_{\ell m}$  of the observation, an estimation  $\hat{s}_{\ell m}$  of the signal is given by:

$$\hat{s}_{\ell m} = \frac{C_{\ell}^s}{C_{\ell}^s + C_{\ell}^n} d_{\ell m}, \quad (2.37)$$

where  $C_{\ell}^s$  and  $C_{\ell}^n$  correspond to the power spectrum of signal and noise respectively. The Wiener filter is the fraction multiplying the  $d_{\ell m}$  coefficients.

The power spectrum of the Wiener filter reconstruction is biased towards values lower than the true signal, with the bias depending on the signal-to-noise ratio of the data [17]. Using equation (2.37), the expected value of the power spectrum for the reconstructed signal is given by

$$\langle C_{\ell}^{\hat{s}} \rangle = \frac{(C_{\ell}^s)^2}{C_{\ell}^s + C_{\ell}^n} < C_{\ell}^s. \quad (2.38)$$

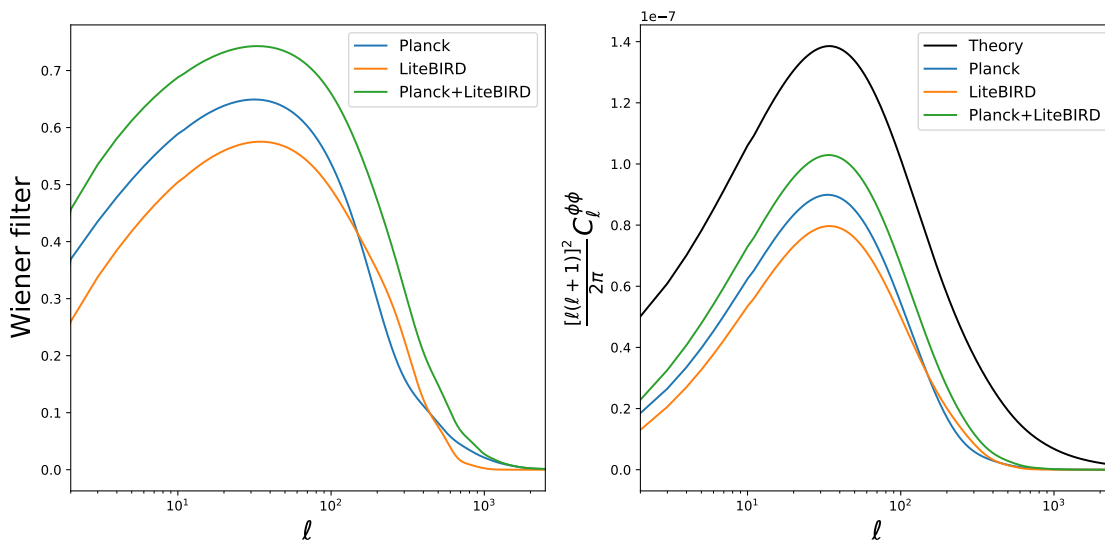


Figure 2.13: *Left: Plots of the Wiener filter corresponding to the minimum-variance estimators of the lensing potential. Right: Plots of the expected value of the reconstructed lensing power spectrum from the minimum-variance estimators for the different experiments considered.*

In Figure 2.13, we can observe how the Wiener filter works when applied to the lensing reconstruction. At low  $\ell$  (large scales) the filter scales the observation by a value lower

than one and, at high  $\ell$  (small scales), the filter rapidly takes a value close to zero due to the dominance of noise. Basically, we are eliminating the noise-dominated scales and keeping only information from scales where the intensity of the signal is relevant compared to the noise. The bias observed after applying a Wiener filter is significant, recovering a considerably lower signal compared to that of the theoretical lensing power spectrum. It is important to take into account that all the plots in Figure 2.13 use the noise levels estimated from the minimum-variance estimator of the lensing potential, which are the best estimation of the lensing angular power spectrum from each experiment. This Figure shows another prove of how combining data from *Planck* and LiteBIRD experiments results beneficial at all scales in the recovery of the lensing spectrum, reducing the observed bias after applying the Wiener filter.

The Wiener filter is applied when dealing with CMB maps, as occurs in several parts of the project, for instance, when working with deflection maps in Chapter 3.

# Chapter 3

## Results

In this chapter we are going to analyse two different situations. First, in Section 3.1, we will consider *Planck* and LiteBIRD experiments only affected by limited angular resolution and instrumental noise. Secondly, in Section 3.2, we will show the effect of the introduction of a mask on the TT quadratic estimator for the *Planck* and LiteBIRD combination. The aim in both situations is to study how well can we recover the lensing gravitational potential.

### 3.1 Lensing reconstruction from noisy and limited resolution experiments

In this Section, we will consider simulations of *Planck*, LiteBIRD, and the combination of both experiments. These simulations consider idealized full-sky experiments only affected by limited angular resolution and white instrumental noise.

In Figures 3.1, 3.2, and 3.3, respectively, the lensing reconstruction for *Planck*, LiteBIRD, and the combination of both are plotted. For each plot there are five different lensing reconstructions in which the TT, TE, EE, TB, and EB quadratic estimators have been used. Additionally, the minimum-variance estimator MV has been plotted, which basically takes the best of each different measurement available of the lensing reconstruction. A very useful plot is Figure 3.4, which shows the values of the weights for the different estimators and experiments used to calculate the weighted-sum of the minimum-variance estimator from equation (1.27).

The combined analysis of all the Figures presented yields interesting results. First, for *Planck*, the best lensing reconstruction comes from the TT estimator, which can be also confirmed from the contribution of more than a 50% at all scales to the MV estimator. It is followed by the TE and EE estimators, which contribute around a 20% to the MV estimator at the low  $\ell$  region. The contributions to the MV estimator from the TB and EB are almost negligible due to the dominance of the reconstruction noise.

A completely contrary situation is faced when looking at the results from LiteBIRD. The major contribution comes from the EB estimator at  $\ell \lesssim 1000$ . For  $\ell \gtrsim 1500$ , the major contribution to the lensing reconstruction signal comes from the TT. However, as this last region is mostly noise dominated, not much signal could be obtained from the

### 3.1. LENSING RECONSTRUCTION FROM NOISY AND LIMITED RESOLUTION EXPERIMENTS

data. The TB estimator is the second with a significant contribution to the MV estimator of the LiteBIRD experiment. The remaining estimators have a minor impact in the lensing reconstruction.

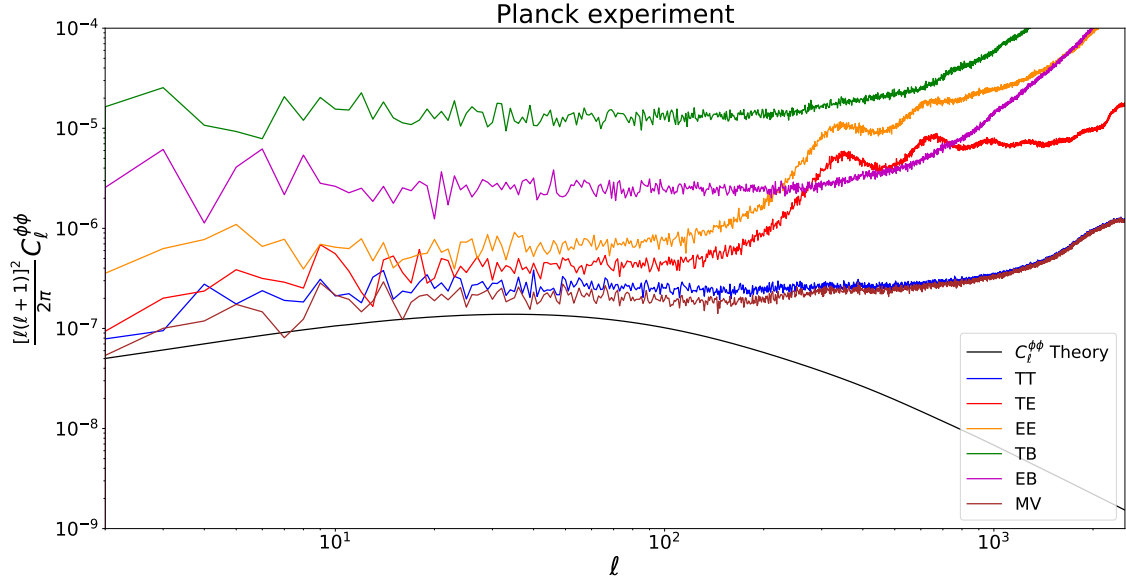


Figure 3.1: Plots of the lensing reconstruction using simulations of the Planck experiment.

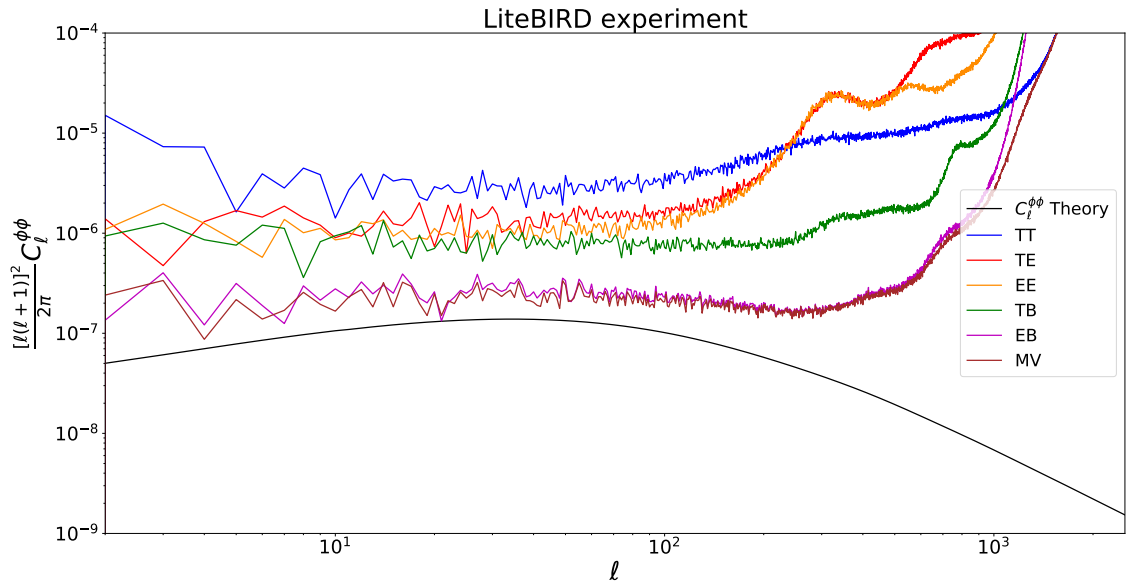


Figure 3.2: Plots of the lensing reconstruction using simulations of the LiteBIRD experiment.

From the *Planck* and LiteBIRD analysis it could be concluded that, in fact, they are complementary experiments. While *Planck* benefits the most from the TT and TE

### 3.1. LENSING RECONSTRUCTION FROM NOISY AND LIMITED RESOLUTION EXPERIMENTS

estimators, the LiteBIRD experiment benefits the most from the EB and TB. This is the underlying reason why a combination of both experiments is perfect.

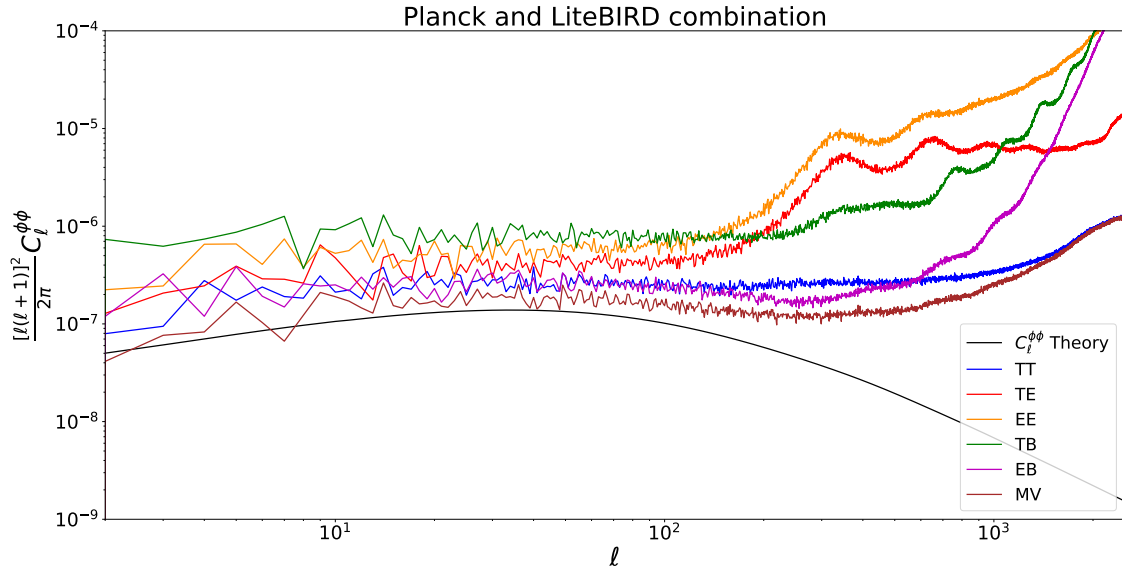


Figure 3.3: Plots of the lensing reconstruction using simulations of the combination of *Planck* and *LiteBIRD* experiments.

The lensing reconstruction from the combination of *Planck* and *LiteBIRD* experiments is better for the TT and EB estimators as it might have been anticipated. In the low  $\ell$  region, the EB estimator dominates, reaching a 60% of the total contribution to the MV estimator, whereas the TT contributes around a 40%. In the high  $\ell$  region, the TT estimator dominates absolutely. Other minor contributions to the MV estimator at low  $\ell$  come from the TE and EE estimators. The remaining quadratic estimators have a minor impact on the MV estimator.

#### 3.1.1 Weights of the minimum-variance estimator

In Figure 3.4, we plot the Okamoto & Hu weights used for the computation of the minimum-variance estimator in Figures 3.1, 3.2, and 3.3. To compute this weights we have used equation (1.34) [1]. Note that in Figure 3.4, for multipoles  $\ell > 500$  we get negative weights for the TE estimator in all the three experiments considered. We do not obtain very negative weights, being the minimum weight obtained  $-0.013$ . Additionally, for the *LiteBIRD* experiment, the TT weights for certain multipoles take values above one.

The multipole region where these negative weights appear is for  $\ell > 500$ , which is noise dominated and no lensing signal is expected to be recovered. In fact, after applying a Wiener filter, the multipole region corresponding to  $\ell > 500$  is highly suppressed. Therefore, we are working effectively always with positive weights.

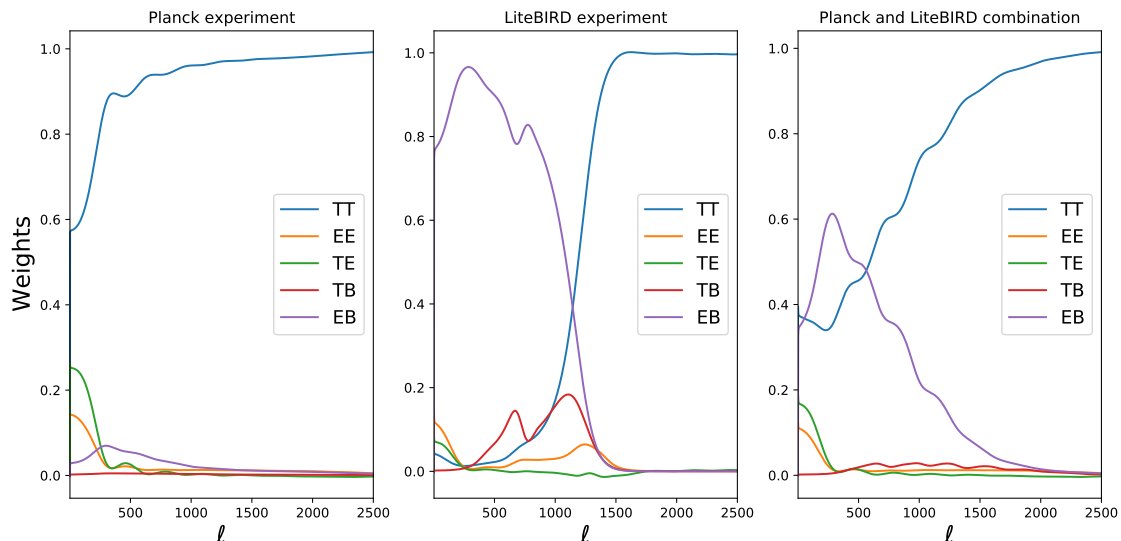


Figure 3.4: Plots of the weights used in the computation of the MV estimator and calculated using Okamoto & Hu weights from equation (1.34).

### 3.1.2 Patch of the reconstructed lensing map

The objective of this Section is to visually compare the original lensing-deflection map with the reconstructed lensing-deflection map. To do so,  $20 \times 20$  degree patches of the lensing-deflection maps centred at  $\theta = \varphi = 0$  are plotted. The lensing-deflection map,  $d_{\ell m}$ , is related to the lensing potential map,  $\phi_{\ell m}$ , by the following equation:

$$d_{\ell m} = \sqrt{\ell(\ell + 1)}\phi_{\ell m}. \quad (3.1)$$

Except the original lensing-deflection map, which is not affected by noise or limited angular resolution, the patches plotted here have been Wiener filtered as explained in Section 2.4.

In Figure 3.5, the different lensing-deflection maps reconstructed using the quadratic estimators and experiments available. For reference, the original lensing-deflection map is plotted in Figure 3.6.

From Figure 3.5, focusing in Planck's maps, we can conclude that the main contributions to the MV estimator comes from the TT, EE, and TE. The TT map is the one that contributes the most to the final shape of the MV map. This is coherent with the weights presented in Subsection 3.1.1. It is particularly interesting how combining the different quadratic estimators to form the MV estimator leads to a clearly better result.

Continuing with LiteBIRD, two major differences with *Planck* can be observed. First, the LiteBIRD's MV reconstruction is better than *Planck*'s. Sharper forms can be observed compared to the original lensing-deflection map. Secondly, not a huge difference is observed between the EB and MV recovered maps, which is compatible with EB being the estimator with the greatest  $S/N$ . The TB is the second map which the highest contribution.

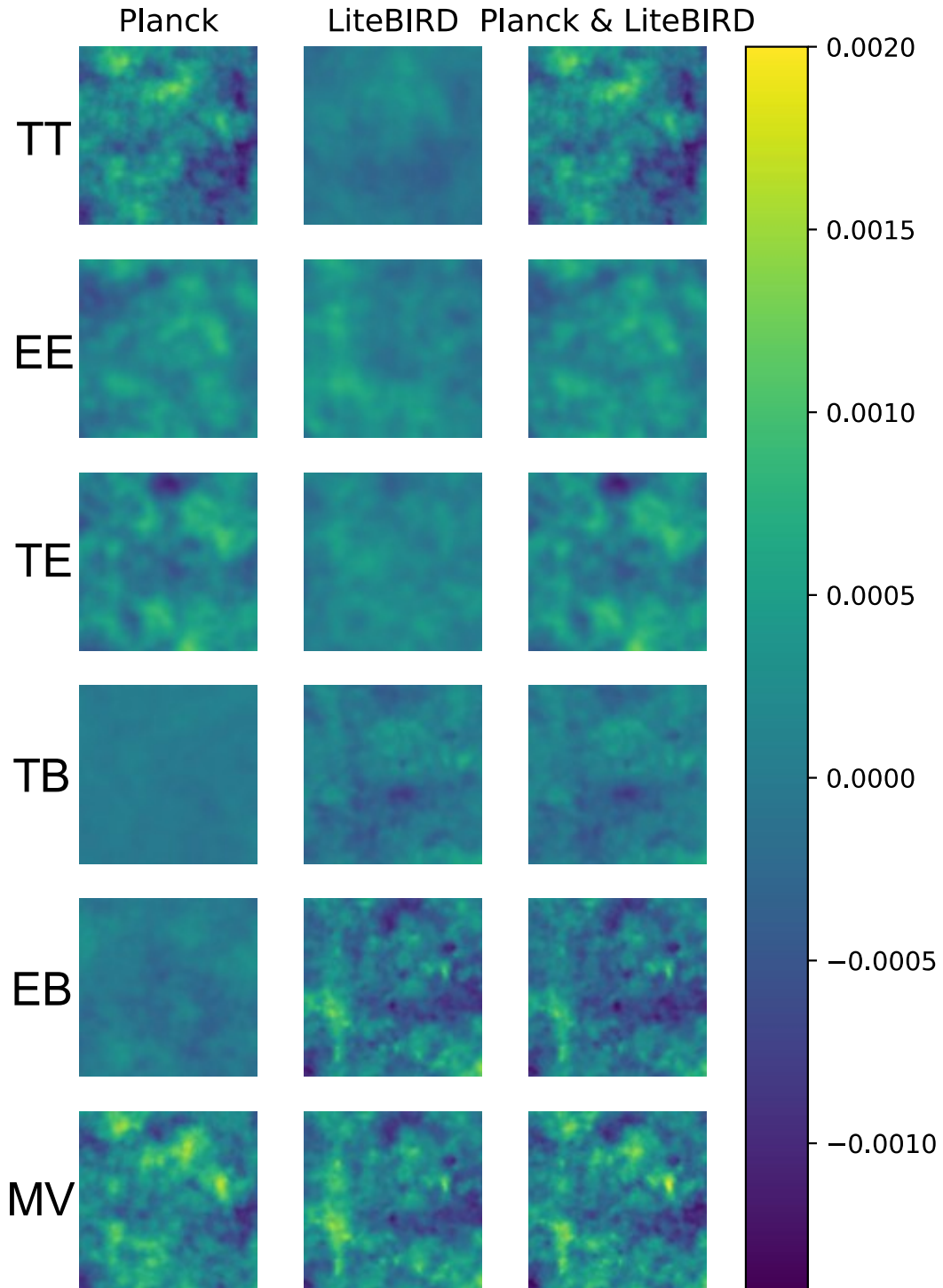


Figure 3.5:  $20 \times 20$  degree central patches of the recovered lensing-deflection map by the different quadratic estimators and experiments.

Finally, we are going to analyse the reconstructed lensing-deflection maps for the combination of *Planck* and LiteBIRD. As explained in previous Sections and shown in Figure

3.5, *Planck* contribution comes mostly from the TT estimator and LiteBIRD most important contribution is the EB estimator. This is what we see for the combination of both experiments in Figure 3.5, the TT map is *Planck*'s and the EB map is LiteBIRD's. It is interesting also that different information is obtained from the TT and the EB maps, contributing both to the MV map. The MV map reconstructed using the combination of both experiments is the best lensing-deflection reconstruction of all those plotted in this Subsection when compared with the original lensing map in Figure 3.6.

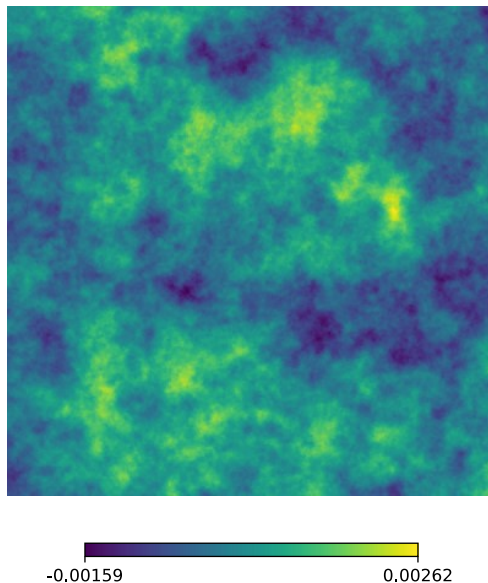


Figure 3.6:  $20 \times 20$  degree central patch of the original lensing-deflection map.

### 3.1.3 Signal-to-noise ratio

In this Section, we compute the signal-to-noise ratio for the lensing potential reconstruction and for the cross-correlation between the lensing potential reconstruction and the original lensing potential map.

The signal-to-noise ratio,  $S/N$ , is calculated using the following equation:

$$S/N = \left( \sum_{\ell} \frac{s_{\ell}^2}{\sigma_{\ell}^2} \right)^{1/2}, \quad (3.2)$$

where  $s_{\ell}$  is the observed signal and  $\sigma_{\ell}$  is the uncertainty associated with the measurement of the signal.

The signal-to-noise ratio for the lensing potential reconstruction,  $\hat{\phi}$ , is calculated using equation

$$S/N = \left( \sum_{\ell} \frac{(C_{\ell}^{\hat{\phi}\hat{\phi}} - N_{\ell})^2}{(C_{\ell}^{\hat{\phi}\hat{\phi}})^2} (\ell + 0.5) \right)^{1/2}, \quad (3.3)$$

### 3.1. LENSING RECONSTRUCTION FROM NOISY AND LIMITED RESOLUTION EXPERIMENTS

where  $C_\ell^{\hat{\phi}\hat{\phi}}$  is the reconstructed lensing angular power spectrum and  $N_\ell$  is the reconstruction noise.

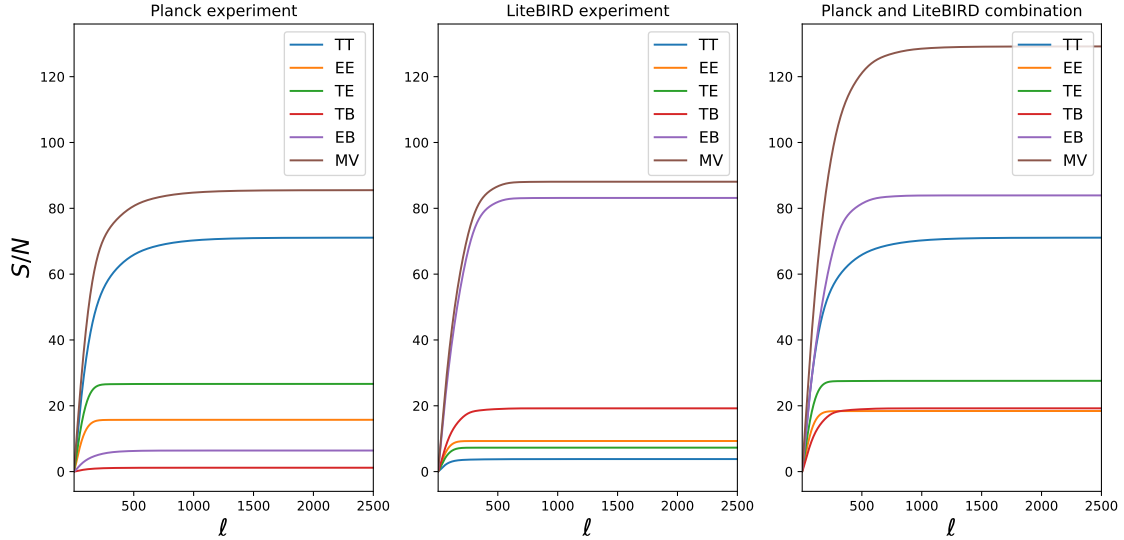


Figure 3.7: Signal-to-noise ratio plots using the theoretical angular power spectra of the signal and the noise.

In Figure 3.7, the theoretical signal-to-noise ratio for the two experiments and their combination are plotted. For *Planck*, the  $S/N$  is dominated by the TT channel as expected, and the MV estimator reaches a  $S/N$  value of 85.51. For LiteBIRD, the  $S/N$  is dominated by the EB channel, and the MV estimator's  $S/N$  is 88.08, which is just a bit higher than the corresponding value for *Planck*'s MV estimator. For the combination of both experiments, the  $S/N$  is considerably higher than for each experiment alone, with the MV estimator reaching a  $S/N$  of value of 129.19. It implies an improvement of about a 50% in the lensing potential reconstruction when combining both experiments. The EB channel is better than the TT, something expected from the plots regarding the individual experiments.

The signal-to-noise ratio for the cross-correlation between the lensing potential reconstruction,  $\hat{\phi}$ , and the original lensing potential map,  $\phi$ , is computed using the following equation:

$$S/N_{\text{correlation}} = \left( \sum_{\ell} \frac{(C_\ell^{\hat{\phi}\hat{\phi}})^2}{C_\ell^{\hat{\phi}\hat{\phi}} C_\ell^{\phi\phi} + (C_\ell^{\hat{\phi}\hat{\phi}})^2} (2\ell + 1) \right)^{1/2}, \quad (3.4)$$

where  $C_\ell^{\hat{\phi}\hat{\phi}}$  is the cross-correlation between the original and reconstructed lensing angular power spectrum and  $C_\ell^{\phi\phi}$  is the original lensing power spectrum.

In Figure 3.8, the signal-to-noise of the cross-correlation for the two experiments and their combination are plotted. We can observe a similar situation, as in Figure 3.7. In an ideal situation we would expect  $C_\ell^{\hat{\phi}\hat{\phi}} = C_\ell^{\phi\phi} = C_\ell^{\phi\phi}$ , so that equation (3.4) transforms to

an monotonically increasing function given by

$$S/N_{\text{perfect correlation}} = \left( \sum_{\ell} (\ell + 0.5) \right)^{1/2}. \quad (3.5)$$

The presence of noise prevents the  $S/N$  to continue growing, leading to the saturation shown in Figure 3.8. The saturation tells us up to which multipole are we able to extract information

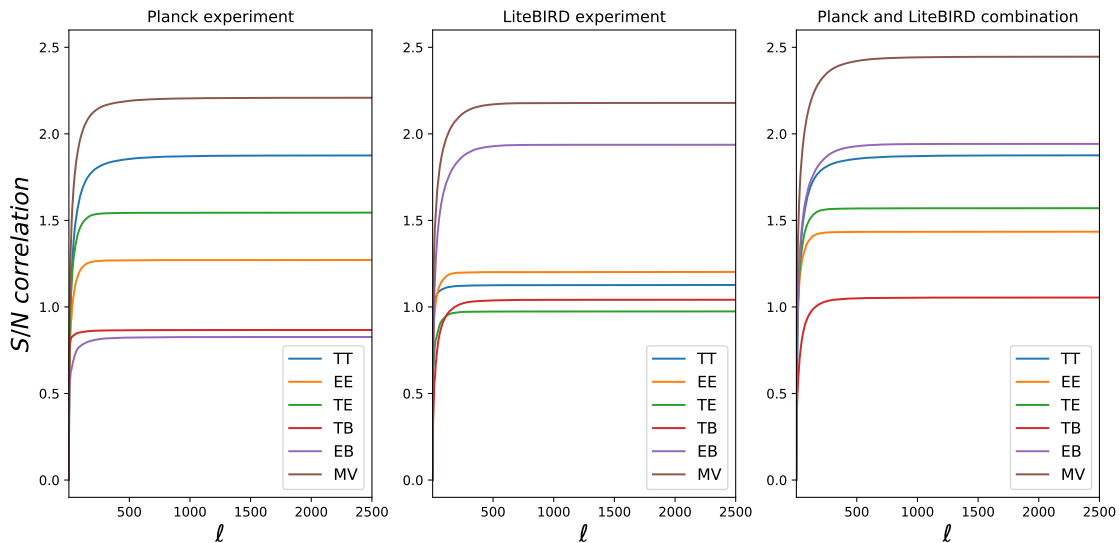


Figure 3.8: *Signal-to-noise ratio plots of the cross-correlation between the original and reconstructed lensing potential.*

## 3.2 Impact of partial sky coverage on lensing reconstruction

In this Section, we present an introduction of the results that can be obtained from the lensing reconstruction of masked CMB maps. Following the steps presented in [13], we apply the TT quadratic estimator to the *Planck* and LiteBIRD combination and show the effect of the mask mean field on the reconstructed lensing power spectrum. Future work will be required to include the rest of the quadratics estimators and more realistic simulations. Both aspects are outside the scope of this work.

In Figure 3.9, the results of applying the TT quadratic estimator to *Planck* and LiteBIRD combination data are presented. We can observe an excess at low multipoles when comparing the reconstructed lensing power spectrum with the expected one. It is caused by the mask mean field due to the presence of the mask. To remove that excess Monte Carlo simulations on unlensed CMB maps should be done as explained in Section 2.2.3.

Figure 3.9 is coherent with the mask mean field presented in Figure 2.9. The mask mean field dominates at  $\ell < 50$ . This multipole range is crucial for lensing because it is the region where most of the lensing power is present.

### 3.2. IMPACT OF PARTIAL SKY COVERAGE ON LENSING RECONSTRUCTION

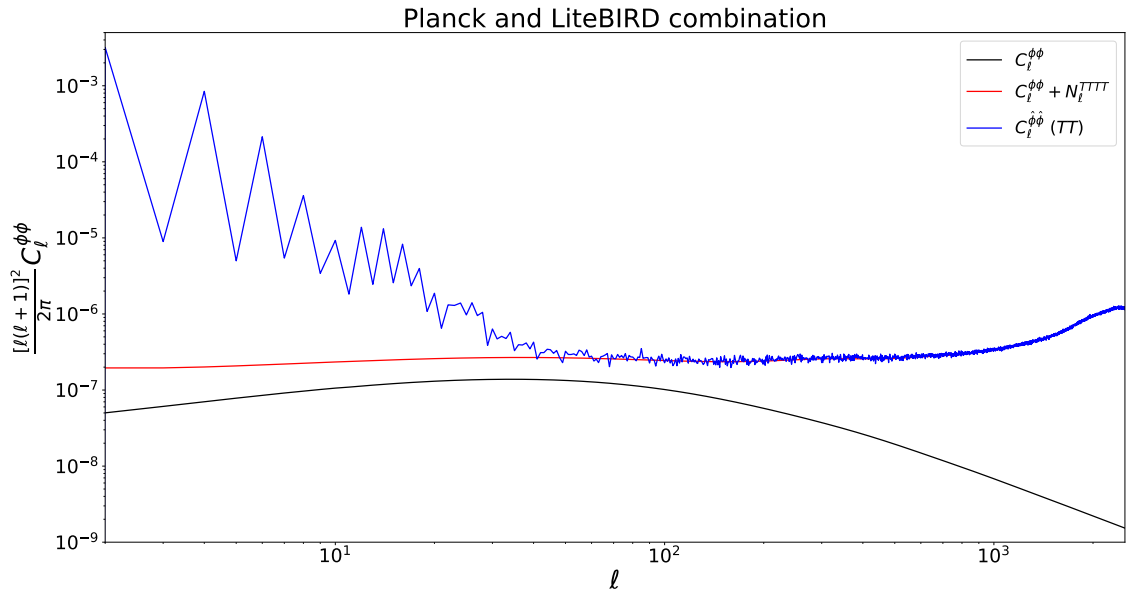


Figure 3.9: Reconstructed lensing power spectrum using the  $TT$  quadratic estimator on the combination of Planck and LiteBIRD. The red line is the theoretical reconstruction and the blue line is the reconstructed lensing power spectrum rescaled by  $f_{gal,4}$ .

## Chapter 4

# Conclusions and future work

In this work, we have focussed in how *Planck* and the future mission LiteBIRD are able to reconstruct the lensing potential from observations of the CMB temperature and polarization. Additionally, a novelty approach of this work is the combination of both experiments. *Planck* is better in CMB temperature, whereas LiteBIRD will be an experiment concentrated on CMB polarization, so combining them is ideal. To do so, different softwares have been used to generate CMB simulations for both experiments and reconstruct the lensing signal.

Five different specialized CMB Python libraries have been utilized. To generate the simulations, the following software was executed: `CLASS` to generate the CMB unlensed and lensed angular power spectra, `healpy` to work with the simulated CMB maps and estimate their angular power spectra, `lenspyx` to lens unlensed CMB maps and, finally, to mask the maps `pymaster` was run. For the lensing reconstruction with quadratic estimators, the library `lensQUEST`, which implements the equations in [1], was run.

The CMB simulations performed in this document only consider three different experimental aspects: instrumental noise, limited angular resolution, and partial sky coverage. It is a simplified scheme where the noise is white, the beam is spherically-symmetric, and the sky-cuts are a Galactic mask with no extragalactic sources. As explained at the start of Chapter 3, we have applied the quadratic estimators to the full-sky and partial-sky simulations separately. The main differences arise from the mode coupling caused by the mask, which produces an additive bias in the lensing signal, named the mask mean field bias, and a multiplicative bias by the coupling matrix. While the multiplicative bias is translated into a normalization factor, the additive one requires estimating the mean field bias, which we have left for future work.

The results show that the data from LiteBIRD mission will be very valuable to constraint the lensing effect. The full-sky signal-to-noise ratio from LiteBIRD ( $\approx 88$ ) is very similar to that obtained from *Planck* ( $\approx 86$ ). However, when combining both experiments it is increased about a 50% to approximately 130. From the weights of the minimum-variance estimator in Figure 3.4, we could observe that for *Planck* experiment the TT estimator is the most important one, whereas for LiteBIRD experiment, it is the EB. A proof of the complementarity of both experiments.

Future work on this project mainly involves improving the CMB simulations in order

---

to make them more realistic. For instance, we can include inhomogeneous noise, the Galactic foregrounds residuals after component separation, and extragalactic foregrounds. The inclusion of extragalactic sources and how to deal with them will require a deeper bibliographic review. Additionally, including higher order biases of the reconstruction noise will be required.

# Bibliography

- [1] T. Okamoto and W. Hu. Cosmic microwave background lensing reconstruction on the full sky. *Physical Review D*, 67(8):083002, April 2003.
- [2] D. J. Fixsen. The temperature of the Cosmic Microwave Background. *The Astrophysical Journal*, 707(2):916–920, 2009.
- [3] R. Durrer. The cosmic microwave background: the history of its experimental investigation and its significance for cosmology. *Classical and Quantum Gravity*, 32(12), 2015.
- [4] A. Lewis and A. Challinor. Weak gravitational lensing of the CMB. *Physics Reports*, 429(1):1–65, June 2006.
- [5] R. Durrer. *The Cosmic Microwave Background*. Cambridge University Press, 2008.
- [6] B. D. Sherwin et al. Two-season Atacama Cosmology Telescope polarimeter lensing power spectrum. *Physical Review D*, 95(12):123529, June 2017.
- [7] K. T. Story et al. A Measurement of the Cosmic Microwave Background Gravitational Lensing Potential from 100 Square Degrees of SPTpol Data. *ApJ*, 810(1):50, September 2015.
- [8] G. Simard et al. Constraints on Cosmological Parameters from the Angular Power Spectrum of a Combined 2500 deg<sup>2</sup> SPT-SZ and Planck Gravitational Lensing Map. *ApJ*, 860(2):137, June 2018.
- [9] Planck Collaboration. Planck 2018 results. VIII. Gravitational lensing. *A&A*, 641:A8, September 2020.
- [10] W. Hu. Weak lensing of the CMB: A harmonic approach. *Physical Review D*, 62(4):043007, August 2000.
- [11] D. Hanson, A. Challinor, G. Efstathiou, and P. Bielewicz. CMB temperature lensing power reconstruction. *Physical Review D*, 83(4):043005, February 2011.
- [12] D. Beck. *Challenges in CMB Lensing Data Analysis and Scientific Exploitation of Current and Future CMB Polarization Experiments*. Theses, Université Paris Cité, October 2019.
- [13] A. Benoit-Lévy, T. Déchelette, K. Benabed, J. F. Cardoso, D. Hanson, and S. Prunet. Full-sky CMB lensing reconstruction in presence of sky-cuts. *A&A*, 555:A37, July 2013.

- [14] D. Blas, J. Lesgourgues, and T. Tram. The Cosmic Linear Anisotropy Solving System (CLASS). Part II: Approximation schemes. *Journal of Cosmology and Astroparticle Physics*, 2011(07):034–034, Jul 2011.
- [15] Planck Collaboration. Planck 2018 results. VI. Cosmological parameters. *A&A*, 641:A6, September 2020.
- [16] S. Bird, M. Viel, and M. G. Haehnelt. Massive neutrinos and the non-linear matter power spectrum. *MNRAS*, 420(3):2551–2561, March 2012.
- [17] R. B. Barreiro, P. Vielva, C. Hernandez-Monteagudo, and E. Martinez-Gonzalez. A Linear Filter to Reconstruct the ISW Effect From CMB and LSS Observations. *IEEE Journal of Selected Topics in Signal Processing*, 2(5):747–754, October 2008.
- [18] A. Lewis, A. Challinor, and D. Hanson. The shape of the CMB lensing bispectrum. *JCAP*, 2011(3):018, March 2011.
- [19] M. Kamionkowski, A. Kosowsky, and A. Stebbins. Statistics of cosmic microwave background polarization. *Physical Review D*, 55(12):7368–7388, 1997.
- [20] A. Zonca et al. healpy: equal area pixelization and spherical harmonics transforms for data on the sphere in Python. *Journal of Open Source Software*, 4(35):1298, March 2019.
- [21] K. M. Górski et al. HEALPix: A Framework for High-Resolution Discretization and Fast Analysis of Data Distributed on the Sphere. *The Astrophysical Journal*, 622:759–771, April 2005.
- [22] G. Fabbian and R. Stompor. High-precision simulations of the weak lensing effect on cosmic microwave background polarization. *A&A*, 556:A109, August 2013.
- [23] A. Lewis. Lensed CMB simulation and parameter estimation. *Physical Review D*, 71(8):083008, April 2005.
- [24] P. Diego-Palazuelos, P. Vielva, E. Martínez-González, and R. B. Barreiro. Comparison of delensing methodologies and assessment of the delensing capabilities of future experiments. *JCAP*, 2020(11):058, November 2020.
- [25] S. Hamimeche and A. Lewis. Likelihood analysis of CMB temperature and polarization power spectra. *Physical Review D*, 77(10):103013, May 2008.
- [26] A. Challinor et al. All-sky convolution for polarimetry experiments. *Physical Review D*, 62(12), Nov 2000.
- [27] Planck Collaboration. Planck 2018 results. I. Overview and the cosmological legacy of Planck. *A&A*, 641:A1, September 2020.
- [28] LiteBIRD Collaboration. LiteBIRD satellite: JAXA’s new strategic L-class mission for all-sky surveys of cosmic microwave background polarization. In *Society of Photo-Optical Instrumentation Engineers (SPIE) Conference Series*, volume 11443 of *Society of Photo-Optical Instrumentation Engineers (SPIE) Conference Series*, page 114432F, December 2020.

- [29] M. Lembo, G. Fabbian, J. Carron, and A. Lewis. CMB lensing reconstruction biases from masking extragalactic sources. *Physical Review D*, 106(2):023525, July 2022.
- [30] D. Alonso, J. Sanchez, A. Slosar, and LSST Dark Energy Science Collaboration. A unified pseudo- $C_\ell$  framework. *MNRAS*, 484(3):4127–4151, April 2019.
- [31] E. Hivon, K. M. Górski, C. B. Netterfield, B. P. Crill, S. Prunet, and F. Hansen. MASTER of the Cosmic Microwave Background Anisotropy Power Spectrum: A Fast Method for Statistical Analysis of Large and Complex Cosmic Microwave Background Data Sets. *ApJ*, 567(1):2–17, March 2002.